

Electronic Theses and Dissertations, 2004-2019

2012

Thermally Annealed Plasmonic Nanostructures

Chaoming Wang
University of Central Florida

 Part of the [Materials Science and Engineering Commons](#)
Find similar works at: <https://stars.library.ucf.edu/etd>
University of Central Florida Libraries <http://library.ucf.edu>

This Doctoral Dissertation (Open Access) is brought to you for free and open access by STARS. It has been accepted for inclusion in Electronic Theses and Dissertations, 2004-2019 by an authorized administrator of STARS. For more information, please contact STARS@ucf.edu.

STARS Citation

Wang, Chaoming, "Thermally Annealed Plasmonic Nanostructures" (2012). *Electronic Theses and Dissertations, 2004-2019*. 2486.
<https://stars.library.ucf.edu/etd/2486>

THERMALLY ANNEALED PLASMONIC NANOSTRUCTURES

by

CHAOMING WANG
B.S. Hubei University, 2004,
M.S. Chinese Academy of Sciences, 2007

A dissertation submitted in partial fulfillment of the requirements
for the degree of Doctor of Philosophy
in the Department of Mechanical, Materials and Aerospace Engineering
in the College of Engineering and Computer Science
at the University of Central Florida
Orlando, Florida

Summer Term
2012

Major Professor: Ming Su

© 2012 Chaoming Wang

ABSTRACT

Localized surface plasmon resonance (LSPR) is induced in metal nanoparticles by resonance between incident photons and conduction electrons in nanoparticles. For noble metal nanoparticles, LSPR can lead to strong absorbance of ultraviolet-violet light. Although it is well known that LSPR depends on the size and shape of nanoparticles, the inter-particle spacing, the dielectric properties of metal and the surrounding medium, the temperature dependence of LSPR is not well understood. By thermally annealing gold nanoparticle arrays formed by nanosphere lithography, a shift of LSPR peak upon heating has been shown. The thermal characteristics of the plasmonic nanoparticles have been further used to detect chemicals such as explosive and mercury vapors, which allow direct visual observation of the presence of mercury vapor, as well as thermal desorption measurements.

Dedicated to

My wife, son and parents

ACKNOWLEDGEMENTS

I would like to take this opportunity to express my sincere gratitude towards my advisor Dr Ming Su, for his help and support throughout my whole study and research. I appreciate his constant guidance, encouragement, and valuable discussion. Meanwhile, I would also like to thank Profs. Kevin Coffey, Jiyu Fang, Patrick K. Schelling and Shengli Zou for serving on my dissertation committee and for their valuable suggestions.

I would like to extend my thanks to Drs. Liyuan Ma and Minghui Zhang for their help on my experimental design and results discussions. I am also thankful for the help from my lab mates Yan Hong, Zeyu Ma, and Mainul Hossain; and my collaborator Haining Wang.

Most of the characterizations were carried out at Materials Characterization Facility (MCF), and NanoScience Technology Center (NSTC). I acknowledged these facilities and also Advanced Materials Processing and Analysis Center (AMPAC) and Department of Mechanical, Materials and Aerospace Engineering (MMAE).

Lastly and most importantly, I thank my wife, my lovely son and our parents for their years of support and understanding. Without their love and spiritual support, it would not have been possible to carry out such a research.

TABLE OF CONTENTS

TABLE OF CONTENTS	vi
LIST OF FIGURES	i
LIST OF TABLES	i
CHAPTER 1: INTRODUCTION	1
1.1 General Overview.....	1
1.2 Motivation.....	5
1.3 Achievement and Organization.....	7
CHAPTER 2: MATERIALS AND METHODS	10
2.1 Introduction.....	10
2.2 Materials and Chemicals.....	10
2.3 Materials Processing and Characterization Techniques	11
2.3.1 Photolithography	11
2.3.2 Thin Film Deposition.....	13
2.3.3 Scanning Electron Microscopy	13
2.3.4 Atomic Force Microscopy.....	15
2.3.5 X-ray Diffraction	17
2.3.6 Energy Dispersive X-ray Spectroscopy.....	18
2.3.7 PID Controller	19
2.3.8 Portable Miniature Spectrometer.....	20
2.4 Experimental Section.....	21
2.4.1 Template Preparation.....	21
2.4.2 Preparation of Periodic Gold Nanoparticle Arrays.....	22
2.2.4 Deposition of Polyelectrolyte Multilayer Films	23

2.2.5 Fabrication of Pattern Using Photolithography	25
2.2.6 Experimental Setup.....	26
CHAPTER 3: FABRICATION AND CHARACTERIZATION OF HIGHLY STALBE GOLD NANOPARTICLE ARRAYS	29
3.1 Introduction.....	29
3.2 Results and Discussion	29
3.2.1 Quality Control of Polystyrene Nanosphere Monolayer	29
3.2.2 Capillary Force Between Colloidal Particles	36
3.2.3 Geometry Calculation of Nanoparticles.....	37
3.2.4 Gold Nanoparticle Arrays on Glass.....	39
3.2.4.1 AFM Characterization.....	39
3.2.4.2 Temperature-induced Shape Changes.....	41
3.2.4.3 Confirmation of Nanoparticle Size and Shape	43
3.2.4.4 Shape Effect on LSPR.....	44
3.2.4.5 Thermal-induced LSPR Peak Shift.....	46
3.2.4.6 Stability of Gold Nanoparticle Arrays	51
3.2.4.7 X-ray Diffraction Characterization.....	52
3.2.5 Gold Nanoparticles Arrays on Quartz	56
3.2.5.1 Thermal-induced Shape Transformation.....	56
3.2.5.2 Temperature Effect on LSPR	58
3.2.5.3 Temperature-dependent Extinction Spectrum	59
3.3 Conclusions	61
CHAPTER 4: THERMAL ANALYSIS BASING ON STABLE GOLD NANOPARTICLE ARRAYS	62
4.1 Introduction.....	62
4.2 Results and Discussion	63
4.2.1 Detection of Wax Adsorption.....	63
4.3.2 Thermal Analysis of Wax Desorption	65
4.3.3 Detection of octadecylamine Absorption and Thermal desorption	69

4.3.4 Detection of DNT Absorption and Thermal Desorption	71
4.3.5 Detection of Thiol Molecular and Thermal Desorption	73
4.3.6 Theoretical Calculation of Detection Sensitivity	77
4.3 Conclusions.....	79
CHAPTER 5: DIRECT VISULIZATION OF MOLECULAR ADSORPTIONS ON GOLD NANOPARTICLE ARRAYS	80
5.1. Introduction.....	80
5.2 Results and Discussion	81
5.2.1 Visualization of Polyelectrolyte Multilayers Adsorption	81
5.2.2 Visualization of 2, 4-Dinitrotoluene Absorption.....	82
5.2.3 Mercury Vapor Detection	85
5.2.4 AFM Measurement.....	87
5.2.5 Optical Microscopic Characterization	88
5.3 Conclusions.....	93
CHAPTER 6: CONCLUSIONS	94
REFERENCES	95

LIST OF FIGURES

Figure 1-1 Schematic illustration of (A) a propagating surface plasmon and (B) a localized surface plasmon.	2
Figure 2-1 Schematic illustration of photolithography using positive and negative photoresist. .	12
Figure 2-2 Schematic diagram of an SEM.	15
Figure 2-3 Schematic diagram of an AFM.	16
Figure 2-4 Principle of X-ray generation.	19
Figure 2-5 A cut-away diagram of an USB4000 spectrometer.	21
Figure 2-6 Schematic of gold nanoparticle arrays fabrication process.	23
Figure 2-7 Chemical structure of poly (allylamine hydrochloride) (PAH) and poly (acrylic acid) (PAA).	24
Figure 2-8 Layer-by-layer deposition of PAH and PAA multilayers.	25
Figure 2-9 Experimental set-up.	26
Figure 3-1 A typical optical microscopic image of self-assembled polystyrene nanosphere on the clean glass surface with different configuration: (1) monolayer; (2) multilayers; (3) under-packed monolayer.	30
Figure 3-2 An optical microscopic image of self-assembled close-packed polystyrene nanosphere monolayer (A); SEM image of polystyrene nanosphere monolayer (B).	31
Figure 3-3 An optical microscopic image of self-assembled polystyrene nanosphere multilayer(A); SEM image of polystyrene nanosphere multilayer (B).....	31
Figure 3-4 An optical microscopic image of self-assembled under-packed polystyrene nanosphere monolayer(A); SEM image of polystyrene nanosphere multilayer (B).....	32
Figure 3-5 Interference between light beams reflected at the air-monolayer and monolayer-substrate plane.	34
Figure 3-6 Theoretical calculation of the volume fraction of close-packed nanospheres monolayer treated as a continuous thin film and the complete film is modeled as an array of	

interconnected hexagonal prisms with the base d_0 (a); the height of the prisms equals the nanosphere diameter d_0 ; the base of the prism equals the diameter of nanospheres (c).	35
Figure 3-7 UV-Vis extinction spectrum of a polystyrene nanospheres monolayer on the glass substrate.	36
Figure 3-8 Schematic illustration of closed-packed polystyrene nanosphere monolayer mask (A); geometry calculation of metallic nanoparticle size (B).	38
Figure 3-9 AFM images of gold nanoparticle arrays on the glass substrate.	39
Figure 3-10 AFM analysis of gold nanoparticles.	40
Figure 3-11 AFM image of gold nanoparticles after polystyrene nanospheres removed and annealed at 300°C for 1 hour.	42
Figure 3-12 AFM image of gold nanoparticles after polystyrene nanospheres removed and annealed at 600°C for 1 hour.	42
Figure 3-13 AFM images of nanohold arrays on the glass substrate after etching off annealed gold nanoparticle arrays.	44
Figure 3-14 Extinction spectra of gold nanoparticle arrays on the glass substrate before (black curve) and after (red curve) annealing.	45
Figure 3-15 Extinction spectra of thermally annealed gold nanoparticle arrays on the glass substrate at different temperature from 30-300 °C (bottom to up).	46
Figure 3-16 LSPR peak shift versus the temperature.	47
Figure 3-17 Theoretical calculated extinction spectra of a gold particle with 50 nm diameter at different temperature from 30 to 200 °C.	49
Figure 3-18 Simulated LSPR peak shift versus the temperature.	51
Figure 3-19 Extinction spectra of annealed gold nanoparticle arrays before (black) and after (red line) putting in ambient condition for 1 month.	52
Figure 3-20 XRD spectra of gold nanoparticles deposited on glass substrate before and after thermal annealing at 300, 400, 500 and 600 °C for 10 hours (from low to high).	53
Figure 3-21 AFM images of gold nanoparticle arrays on the quartz substrate before (A) and after (B) annealing at 600 °C for 10 hours.	57
Figure 3-22 AFM images of nanohold arrays on the glass substrate after etching off high temperature annealed gold nanoparticle arrays.	58
Figure 3-23 Extinction spectra of gold nanoparticle arrays on the quartz substrate before (black curve) and after (red curve) annealing.	59

Figure 3-24 Extinction spectra of gold nanoparticle arrays on quartz substrate under different temperatures.....	60
Figure 4-1 Schematic illustration of ultra-sensitive plasmonic nano-balance.....	63
Figure 4-2 Extinction spectra of gold nanoparticle arrays after exposing to wax vapor for different times.....	64
Figure 4-3 LSPR peak shift versus the thickness of wax films.....	65
Figure 4-4 SPR peak shift of wax coated nanoparticles versus the temperature at different heating rates, where square, circle, and triangle are collected at 2, 5, and 10 °C/min.....	66
Figure 4-5 Plot of $\ln\beta$ versus $-1/T$	69
Figure 4-6 Extinction spectra of gold nanoparticle arrays after exposed to octadecylamine vapor for different times (A), SPR peak shift versus the thickness of octadecylamine thin films (B)....	70
Figure 4-7 LSPR peak shifts upon the desorption of octadecylamine from gold nanoparticles at heating rate of 5 °C /min.....	70
Figure 4-8 (A) Extinction spectra of gold nanoparticles coated by octadecylamine thin films as temperature increases linearly (from low to high); (B) The transmission change of peak intensity of gold nanoparticles covered by octadecylamine versus time as temperature increases.....	71
Figure 4-9 (A) Extinction spectra of gold nanoparticles after exposing to 2,4-dinitrotoluene for a period of time ranging from 5, 10, 15, 20 and 25 seconds (from low to high); (B) The transmission change of peak intensity of gold nanoparticles covered by 2, 4-dinitrotoluene versus time as temperature increases.....	72
Figure 4-10 SPR peak shifts upon desorption of 2, 4-dinitrotoluene from gold nanoparticles at heating rate of 5 °C /min.....	73
Figure 4-11 Extinction spectra of gold nanoparticle arrays in air before (black line) and after (red line) modified by 1, 10-decanedithiol.....	74
Figure 4-12 Extinction spectra of 1, 10-decanedithiol molecules modified gold nanoparticles at different temperatures from 25°C to 300 °C (bottom to up).....	75
Figure 4-13 SPR peak shifts upon the desorption of 1,10-decanedithiol (A) and its corresponding derivative curve (B) from gold nanoparticles at a heating rate of 5 °C /min.....	76
Figure 5-1 Schematic illustrations of color change of gold nanoparticles upon deposition of different molecular thin films (mercury, DNT and polyelectrolyte multilayers).....	81
Figure 5-2 (A) The UV-Visible extinction spectra of gold nanoparticle array with 0 to 3 bilayers of PAH/PAA (bottom to top), respectively; (B) a micrograph of circular patterns that have been covered by three bilayers of PAH/PAA.....	82

Figure 5-3 (A) The extinction spectra of gold nanoparticles after exposing to DNT vapor, where the curves are taken at 0, 5, 10, 15, 20 and 25 seconds (bottom to top), respectively; (B) a micrograph of a circle pattern not exposed to DNT.....84

Figure 5-4 The peak shifts of gold nanoparticles after exposed to 15 ppm mercury vapor (A), where the curves are taken at 0, 1, 2, 5, 10, 30, 60 and 120 min (bottom to up), respectively; (B) the magnitude of peak shifts at different exposure time.87

Figure 5-5 AFM images of nanoparticles before (A) and after (B) exposing to mercury for 120 min, where insets show the according cross section profiles.88

Figure 5-6 An optical micrograph of micropatterns produced in mercury vapor on a patterned substrate with gold nanoparticles, where the relative white areas are not exposed to mercury vapor.....89

Figure 5-7 A micropattern produced on a glass substrate with gold nanoparticles in mercury vapor (B), where the circular area is exposed to mercury vapor; an EDX spectrum collected from a circle micropattern (C) after exposing to mercury vapor.90

Figure 5-8 A graph of “Hg” character after exposing to mercury vapor on a 2×2 cm² glass with an ordered array of gold nanoparticles.90

Figure 5-9 Extinction spectra of gold nanoparticle arrays after exposed to indium vapor for different length of time.....91

Figure 5-10 Extinction spectra of silver nanoparticle arrays after exposed to mercury vapor for different length of time.....92

Figure 5-11 High temperature annealed gold nanoparticle arrays on a 7.5cm × 7.5 cm glass substrate.....93

LIST OF TABLES

Table 3-1 Details of FCC structured crystals.....	55
Table 4-1 Calculated detection sensitivity basing on my experimental results.....	78

CHAPTER 1:INTRODUCTION

1.1 General Overview

Surface plasmon resonance (SPR) is the collective oscillation of valence electrons in a solid material stimulated by incident light. The resonance condition is established when the frequency of photons matches the natural frequency of surface electrons oscillating against the restoring force of positive nuclei. There are two types of SPR as shown in Figure 1-1: (1) propagating surface plasmon polaritons (SPPs) and (2) localized surface plasmon resonance (LSPR). SPPs can be excited on thin metal films using grating or prism couplers, and can propagate hundreds of micrometers along the metal surface with an associated electric field that decays exponentially from the metal film surface (normal to the dielectric-metal interface).¹⁻⁷ Changes in refractive index around the dielectric-metal interface shifts the plasmon resonance, which can be detected as intensity, wavelength or angle shifts.⁸⁻¹¹ LSPR in nanometer-sized structures is dependent on the size and shape of nanoparticles, the inter-particle spacing, the dielectric properties of materials, and the dielectric properties of the surrounding medium.¹²⁻²² When metal nanoparticles are excited by an incident light, the localized surface plasmon resonance occurs, which will result in strong light scattering and generate an intense absorption band.

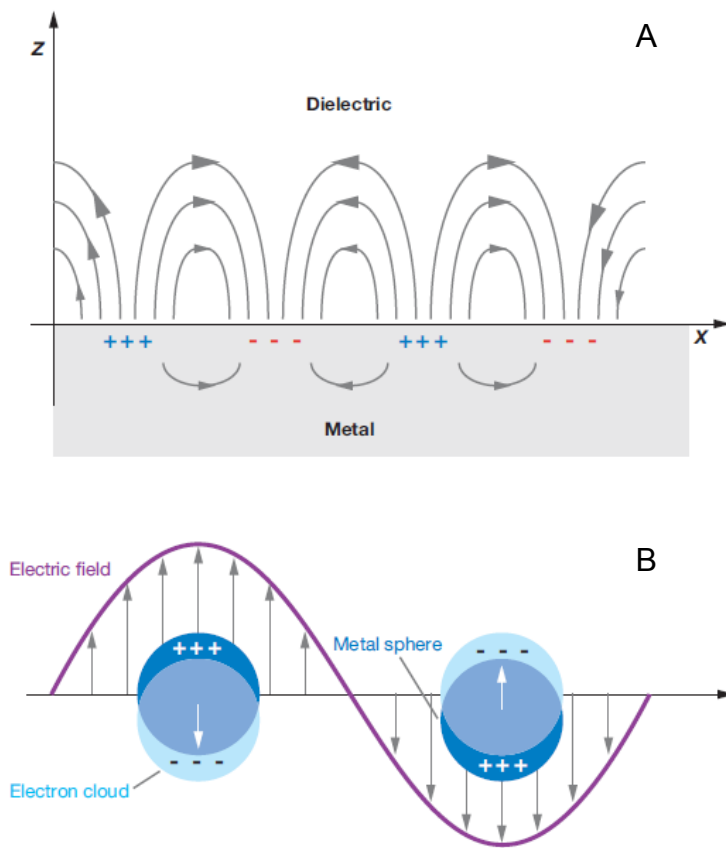


Figure 1-1 Schematic illustration of (A) a propagating surface plasmon and (B) a localized surface plasmon.

When noble metal nanoparticles with a diameter that is much smaller than the wavelength of light are impinged with light, a strong ultraviolet-visible (UV-Vis) absorption band (known as LSPR) exhibits, which is not present in the spectrum of bulk metal. It is one of the signature optical properties of noble metal nanoparticles.

The simplest theoretical approach for modeling the optical properties of metallic nanoparticles is the Mie theory,²³ which is described as

$$E(\lambda) = \frac{24\pi N_A a^3 \varepsilon_m^{3/2}}{\lambda \cdot \ln(10)} \left[\frac{\varepsilon_i}{(\varepsilon_r + \chi \varepsilon_m)^2 + \varepsilon_i^2} \right] \quad (1)$$

where $E(\lambda)$ is the extinction (sum of absorption and scattering), N_A is the density of nanoparticles, a is the radius of metallic nanosphere, ε_m is the dielectric constant of the medium surrounding of the metallic nanosphere, λ is the wavelength of absorbing radiation, ε_i is the imaginary portion of the nanoparticle's dielectric function, ε_r is the real portion of the metallic nanoparticle's dielectric function, and χ is the term that describes the aspect ratio of nanoparticle (equal to 2 for a sphere). The LSPR spectrum of an isolated metallic nanosphere embedded in an external dielectric medium will depend on the nanoparticle radius a , composition of the nanoparticles (ε_i and ε_r), and environment's dielectric constant (ε_m). The peak wavelength λ_{\max} occurs at a certain wavelength, where ε_i is small and $\varepsilon_r = -\chi \varepsilon_m$. For spherical nanoparticles, χ is equal to 2, and the equation is modified such that the peak wavelength λ_{\max} occurs when $\varepsilon_r = -2\varepsilon_m$. As above mentioned, the real part of the dielectric constant of the metal can be negative number. There is a basic relation between the dielectric constant and a constant index of refraction, $\varepsilon = (n + im)^2$, where ε is dielectric constant, n and m is real and imaginary part of refraction index. n is relative to refraction, and m is relative to absorption. The real part of ε (ε_r) equals to $n^2 - m^2$. For dielectric material, when $m=0$, which means there is no absorption, like water and glass. For metal, there is n and m , and when m is larger, $n^2 - m^2$ could be negative, it's normal, like Ag and Au. For nonspherical metallic nanoparticles, the surface plasmons are unevenly distributed around them, manifesting in a shape dependence of the LSPR absorption spectra. The plasmon resonance of metallic nanorods, for example, splits into two peaks: (i) a strongly red-shifted long axis or longitudinal mode (L) (polarization parallel to the long axis), and (ii) a slightly

blue-shifted transverse mode (T) (polarization perpendicular to the long axis).²⁴⁻²⁶ As the aspect ratio of a nanorod increases, the separation between two plasmon bands becomes more pronounced. Triangular metallic nanoparticles exhibit multiple plasmon resonances, which is due to dipole, quadrupole or higher multimode oscillations.²⁷

Numerical methods including the T-matrix method, discrete dipole approximation (DDA), finite-difference time domain (FDTD) simulations, and finite element calculations have to be used to derive resonant frequencies, absorption, extinction, and scattering efficiencies of non-spherical particles by calculation of the frequency dependence of ϵ_r and ϵ_i .²⁸⁻³¹ Among these, the DDA method, which combines coefficient algorithms and inexpensive computing capability, has been used commonly to derive scattering and absorption properties of objects with arbitrary size and geometry.

The LSPR of well controlled metallic nanoparticles or nanostructures can be tuned very broadly (from optical wavelengths of 400 to 900nm) by precisely controlling their size, shape and composition using different chemical and lithographic methods.³²⁻³⁶ Nanostructures can be made with either top-down or bottom-up approaches.³⁷⁻⁴⁰ Top-down techniques include using diverse conventional lithographic techniques to make patterned nanostructures (e.g., on a planar substrate), while bottom-up methods use chemical methods in conjugation with process kinetics or dynamics, to assemble nanostructures in a solution or on substrates.

1.2 Motivation

Thermogravimetric analysis (TGA) can determine a material's thermal stability and its fraction of volatile components by monitoring its weight change during programmed temperature rise processes.^{41, 42} The mass loss recorded by an electronic or mechanical balance is used to derive the point where the mass loss is apparent.⁴³ The detection sensitivity of thermogravimetric analysis is strongly dependent on the precision of the mass measurements. Historically, precise mass measurements have been achieved in mechanical balances through three designs: a sharp knife edge as frictional-free fulcrum, a long pointer to amplify the deviation of beam, and a long lever that allows fractional mass to be applied. An electronic balance offers much higher precision and accuracy using a device called strain gauge load cell.⁴⁴ As the cell is compressed, the electrical resistance changes, which is measured by Wheatstone bridge. In the absence of turbulent airflow, the detection sensitivity of an electronic balance can reach 1 μg at room temperature. As temperature increases, natural convection from air currents negatively affects the precision. The mass of material can also be measured in dynamic mode, where the resonance frequency of a solid beam or surface shifts once a mass is added on top of it. Quartz crystal microbalances (QCM) can measure the weight of deposited mass at high sensitivity (0.2 μg) in ambient conditions.⁴⁵ Micro-fabricated cantilevers operating in dynamic mode can detect as less as 8 ng by reducing the size of the vibrating elements.⁴⁶ One-dimensional nanomaterials such as nanotubes and nanowires have been proposed as the beams for the dynamic mass measurements.⁴⁷⁻⁴⁹ Owing to the small mass of a single nanotube or nanowire, the frequency shift upon the loading of the material will be significant, meaning that the detection sensitivity

could be very high to reach the single molecule level. However, the mass readout from a single nanotube/wire is challenging, and requires sophisticated techniques such as electron microscopy, thus cannot be widely used for mass measurement.⁵⁰⁻⁵⁵ In the case of the micro-cantilever balance, loading testing samples on the active area requires a micromanipulator and is time-consuming.⁵⁶ Most importantly, the available low-cost and sensitive mass measurement techniques are not compatible with thermal analysis, where the sensing elements cannot survive high temperatures, or the temperature effect is nonlinear or too large to identify mass measurement signals.

The advent of nanostructured materials has created many opportunities to dramatically enhance the ability to detect adsorbed chemicals. Nanoparticles with unique optical, magnetic, electronic, and chemical properties have been used either alone or as functional additives to improve performance for molecular detection, where changes in the physical properties of nanoparticles reflect the existences or concentrations of target molecules.⁵⁷⁻⁶⁷ Owing to the small size and large surface area of nanoparticles, the detection sensitivity is enhanced and response time is shortened.⁶⁸⁻⁷⁰ In particular, nanoparticles of noble metals including gold and silver have shown strong surface plasmonic effects. Once these nanoparticles are assembled to form an ordered array on a dielectric substrate, an incoming white light can excite the surface plasmons, which coherently resonate with those of nearby nanoparticles, causing extinction or scattering of light with improved efficiency. The LSPR peaks shift upon adsorption of molecules due to changes in the dielectric constant of the local medium, which gives a mean of signal transduction to detect the adsorbed chemicals with highly sensitivity.⁷¹⁻⁷⁴ However, a major issue using LSPR for chemical detection like this way is the limited uses in extreme environmental conditions,

such as high working temperature, dangerous spaces that are filled with toxic or explosive species, etc., which are very common in industrial processes. One particular area of interest is the detection of mercury vapor, which can affect the lungs, kidneys, skin, and eyes, nervous, and immune systems of humans.⁷⁵⁻⁷⁷ As mercury containing products (i.e., fluorescent lighting) and industrial processes (i.e., coal burning power generation and solid waste incineration) become more and more popular, there is the need to conveniently detect mercury vapor in air over a large area.^{78, 79} Another particular area of interest is the detection of explosives due to their extensive security and life problems for humans and the ecosystem.⁸⁰⁻⁸² The production, storage and testing of explosives and their use in terrorist and war activities has led to the contamination of soil with nitro aromatic explosive molecules such as TNT (2, 4, 6-trinitrotoluene) and their derivatives. Thus it is required to develop an easy and cost effective way to detect those explosive species.

Although each of above-mentioned methods has certain advantages, many of them are time-consuming, labor-intensive, require relatively expensive instrumentation and are not readily useful for field determinations. Thus, active research is being pursued for the development of simple and field-portable analytical methods to yield better sensitivity in the detection of trace levels of nitro aromatic explosive compounds.

1.3 Achievement and Organization

The focus of this work is the fabrication and applications of thermally annealed stable ordered gold nanoparticle arrays for chemical sensing.

The first originality of my research is the fabrication and thermal annealing of ordered arrays of gold nanoparticles. It has been an issue that changes (instability) in the optical properties of gold nanoparticles due to morphological changes that occur upon exposure to solvent, analyte or drying introduce uncertainty in molecular detection based on refractive index. The preparation of highly stable nanoparticles with robust plasmonic properties has been challenging. I have used a simple and low-cost method to make stable gold nanoparticle arrays with robust plasmonic properties on glass or quartz substrates by a combination of nanosphere lithography and thermal annealing. The width and intensity of the extinction peak (at 563 nm) becomes narrower and stronger after annealing due to the stabilizing effect of the glass matrix on the morphology of partially embedded gold nanoparticles. As their temperature increases, the extinction peak of the annealed gold nanoparticles shifts to long wavelength direction gradually. A linear response exists between peak shift and temperature. The plasmonic peak returns to its original position after sample is cooled down.

The second originality of my research is that the thermal plasmonic properties of the gold nanoparticles can be used to perform novel thermal analysis of adsorbed organic molecules. In the so-named plasmonic nano-balance, extinction peaks of gold nanoparticles shift linearly as mass of material is loaded on the nanoparticles. Temperature induced material desorption leads to the recovery of extinction peak to its original position. Sub-nano-gram sensitivity has been achieved on nanoparticle arrays in ambient condition. Such high mass detection sensitivity, combined with remote detection ability and high temperature operation of plasmonic sensors, could allow in-situ detections of masses of materials and molecules, and the stand-off mass detection of explosive materials.

The third originality of my research is that low concentrations of molecules (polymer, mercury vapor or explosive) can be detected directly by visual color changes of an ordered array of thermally annealed gold nanoparticles. The adsorption of molecules onto gold nanoparticles changes the local dielectric constant, and the optical appearance of the glass substrates. In the case of mercury vapor, chronic exposure to mercury can cause the formation of gold-mercury alloy, and the color change of a plasmonic gold nanoparticle array. The amalgamated nanoparticles can be regenerated by heating to 300°C, thus providing a low cost and convenient way to detect mercury vapor. In addition, explosive vapor condenses on the solid surface of the nanoparticles, the changes local dielectric constant and leads to color change of substrate. At last, polymer multilayers that have precisely controlled thicknesses have been used as a standard to calibrate the detection capability of this method.

This work is organized as the following sequences. Chapter 1 presents the theoretical background of LSPR and the motivation of my research. Chapter 2 shows the fabrication and characterization techniques of stable gold nanoparticle arrays. Chapter 3 shows thermal tailoring and characterization of gold nanoparticle arrays on transparent glass or quartz substrate. Chapter 4 describes how the fabricated plasmonic gold nanoparticle arrays can be used to perform novel thermal analysis of adsorbed organic molecules. Chapter 5 shows that the adsorption of explosive or toxic molecules on plasmonic gold nanoparticles arrays can be observed visually using naked eyes. Chapter 6 summarizes the conclusions of this research.

CHAPTER 2: MATERIALS AND METHODS

2.1 Introduction

Nanosphere lithography has been used to make ordered arrays of gold nanoparticles on glass or quartz substrates, where a polystyrene nanosphere monolayer is used as a mask for metal thin film evaporation. Samples before and after annealing have been characterized by atomic force microscopy and X-ray diffraction. The substrate with a gold nanoparticle array is fixed onto a custom-made cell and a resistive heating wire coupled with proportional-integration-differentiation (PID) controller is used to heat or cool the sample with a pre-designed program. The optical spectra are collected in transmission mode using a miniature optical fiber spectrometer and processed with commercial software.

2.2 Materials and Chemicals

All chemicals used are of reagent grade and used without further purification. Borosilicate glass microscope slides, paraffin, 2, 4-dinitrotoluene (DNT), octadecylamine and mercury are obtained from VWR (West Chester, PA). Surfactant-free carboxyl-modified polystyrene suspension (400nm diameter) is obtained from Invitrogen (Carlsbad, CA) which contains 4% solid. Ultrapure water with resistivity of $18.2 \text{ M}\Omega \text{ cm}^{-1}$ is obtained from a Millipore system (Marlborough, MA), and used to clean glass surfaces, and make solutions. High purity silver microwires (99.99%) obtained from Goodfellow (Oakdale, PA) is used as the source

material in the thermal evaporations. Polyacrylic acid (PAA) with molecular weight of 90,000 and polyallylamine hydrochloride (PAH) with molecular weight of 70,000 are purchased from Polysciences and Aldrich, respectively. 1, 10-decanedithiol is purchased from Aldrich (Milwaukee, WI), and absolute ethanol is obtained Ricca (Arlington, TX). Mercury is used by delivering their mercury vapor into the detection chamber using a continuous flow of nitrogen.

2.3 Materials Processing and Characterization Techniques

2.3.1 Photolithography

Photolithography is the process used to pattern silicon in the fabrication of microelectronic devices. The process involves several steps, which are shown in Figure 2-1. First, a photoresist is spin-coated on a clean substrate and baked at a moderate temperature to remove the solvent. Secondly, a patterned photo-mask is aligned with the substrate followed by brief exposure to UV light for a certain time. Thirdly, the UV light exposed substrates are developed by immersing into a type of developer solution, which is determined by the type of photoresist chosen. After this, the desired mask pattern will be left on the substrate surface depending on what type of the photoresist was used.

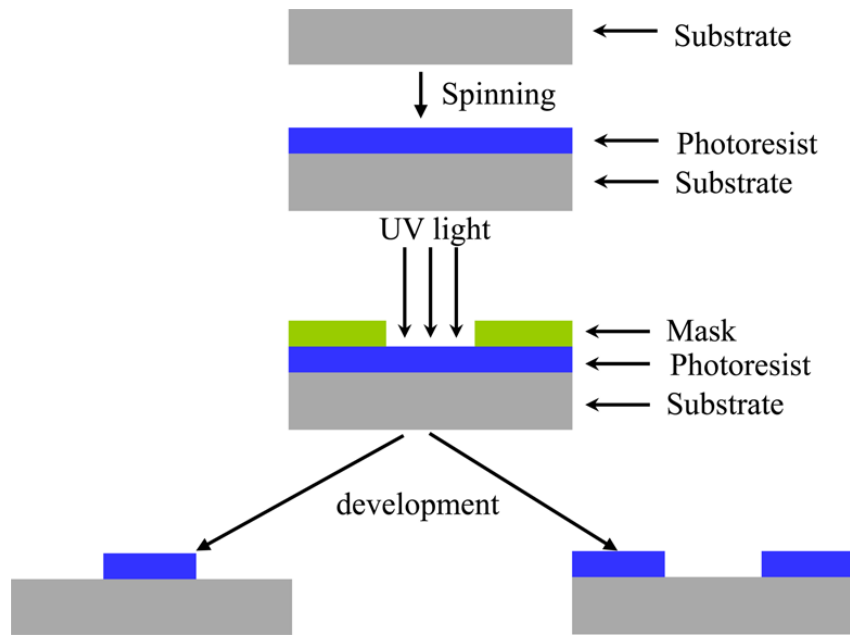


Figure 2-1 Schematic illustration of photolithography using positive and negative photoresist.

Photoresists are light sensitive organic compounds that will either cross-link or undergo degradation when exposed to light. A positive resist is a type of photoresist in which the portion of the photoresist that is exposed to light becomes soluble to the photoresist developer. The portion of the photoresist that is unexposed remains insoluble to the photoresist developer. A negative resist is a type of photoresist in which the portion of the photoresist that is exposed to light becomes insoluble to the photoresist developer. The unexposed portion of the photoresist is dissolved by the photoresist developer. The mask is typically made of quartz and is defined using evaporated chromium to make some areas opaque. Thus, some regions of the photoresist are protected from light and do not cross-link or degrade. A suitable solvent is used to dissolve the non-cross-linked resist after exposure, leaving behind patterned features.

2.3.2 Thin Film Deposition

Thin film deposition of metallic, insulating, conductive and dielectric materials plays an important role in a large number of manufacturing, production and research applications. Thermal evaporation, sputtering and electron beam evaporation are the processes most widely used for the deposition of thin films. A thermal evaporator uses an electric resistance heater to melt the material and raise its vapor pressure to a useful range. An electron beam evaporator extracts a high-energy beam from an electron gun to boil a small spot of material. The deposition process is done in a high vacuum, both to allow the vapor to reach the substrate without reacting with or scattering against other gas-phase atoms in the chamber, and reduce the incorporation of impurities from the residual gas in the vacuum chamber. Sputtering relies on a plasma (usually a noble gas, such as argon) to knock atoms of a "target" material, a few atoms at a time. Not only for single element deposition, it is also useful for compounds or mixtures, where different components would otherwise tend to evaporate at different rates.

2.3.3 Scanning Electron Microscopy

A scanning electron microscope (SEM) is a microscope that images a sample by scanning its surface with an electrons beam in a raster scan pattern. When the electrons interact with atoms that make up the sample, it will produce signals that contain information about the sample's surface topography, composition, and other properties. Compared to traditional microscopes, SEM has large depth of field and higher resolution, which allows more of a specimen to be in focus at one time and provides a much higher level of magnification.

For a typical SEM (see Figure 2-2), an electron beam is emitted from a thermionic or field emission electron gun. The electron beam, which typically has an energy ranging from 0.2 keV to 40 keV, depending on the acceleration voltage, is focused by two magnetic condenser lenses to a spot about 0.4 to 5 nm in diameter. The electron beam passes through pairs of scanning coils in the electron column, typically in the final lens, which deflect the beam in the x and y axis so that it will scan in a raster fashion over a rectangular area on the surface of sample. When the primary electron beam interacts with the sample, the electrons lose energy by repeated random scattering and absorption within a teardrop-shaped volume of the specimen, which is known as the interaction volume and can extend from less than 100 nm to around 5 μm into the surface. The size of the interaction volume depends on the electron's landing energy, the atomic number of the specimen and the specimen's density. The energy exchange between the electron beam and the sample results in the reflection of high-energy electrons by elastic scattering, emission of secondary electrons by inelastic scattering and the emission of electromagnetic radiation, each of which can be detected by specialized detectors. Electronic amplifiers of various types are used to amplify the signals, which are displayed as variations in brightness on a computer monitor. Each pixel of computer video memory is synchronized with the position of the beam on the specimen in the microscope, and the resulting image is therefore a distribution map of the intensity of the signal being emitted from the scanned area of the specimen.

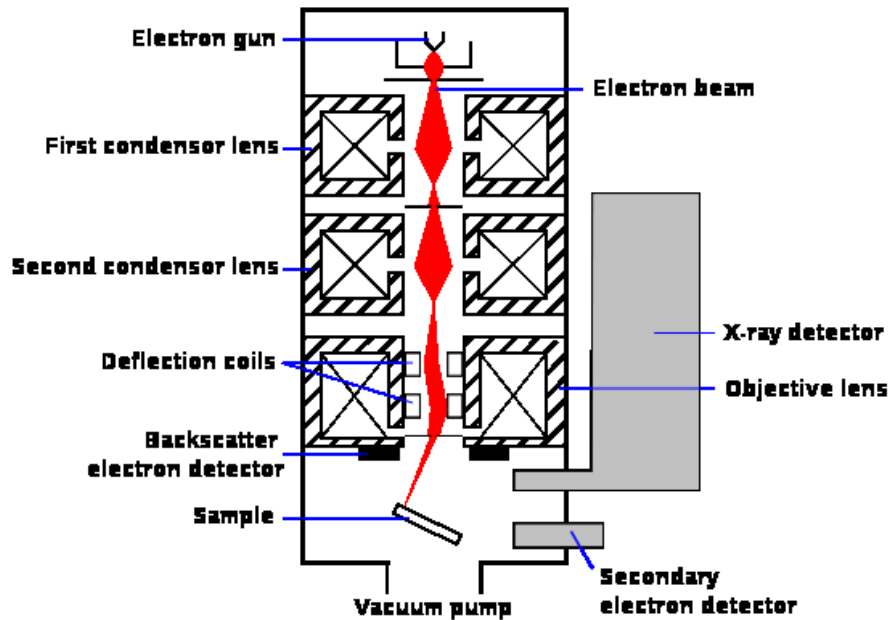


Figure 2-2 Schematic diagram of an SEM.

2.3.4 Atomic Force Microscopy

Atomic force microscopy (AFM), as shown in Figure 2-3, consists of a cantilever with a sharp tip (probe) at its end that is used to scan the surface of the specimen. The cantilever is typically made of silicon or silicon nitride with a tip radius of curvature on the order of nanometers. When the tip is brought into proximity of a sample surface, forces between the tip and the sample lead to a deflection of the cantilever according to Hooke's law. Depending on instrument design, the forces that are measured in AFM include mechanical contact force, van der Waals forces, capillary forces, chemical bonding, electrostatic forces, magnetic forces, Casimir forces, solvation forces, etc. In AFM, the deflection is measured using a laser spot

reflected from top surface of the cantilever, which has been coated with a thin layer metallic film (normally gold), into an array of photodiodes.

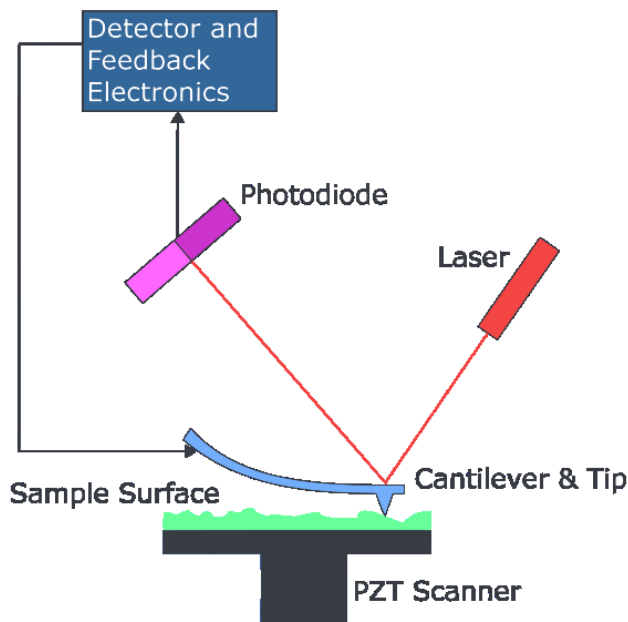


Figure 2-3 Schematic diagram of an AFM.

An AFM can be operated in different modes depending on the application. In general, possible imaging modes are divided into static (also called contact) modes and a variety of dynamic (non-contact or "tapping") modes where the cantilever is vibrated. Meanwhile, it can also be used in conductive mode or liquid mode. An important application of AFM is to obtain the morphology, size, shape and roughness of a sample's surface. All of the imaging parameters, such as scanning size, scanning rate, image resolution, imaging force, and integral gain values can be adjusted during imaging process. Data analysis such as 3D visualization, smoothing, cross section and distribution analyses can be carried out once the image is obtained. Although the

sensitivity of X or Y direction is low because of the tip broadening effect, AFM offers extremely high Z sensitivity, and it is suitable for surface roughness measurement.

2.3.5 X-ray Diffraction

The crystallographic structure of bulk materials, such as salts, metals, minerals, semiconductors, as well as various inorganic, organic and biological molecules, or their metallic nanoparticles, can be determined by X-ray diffraction (XRD). Crystals are constructed by regular arrays of atoms, and X-rays can be considered waves of electromagnetic radiation. It is known that atoms scatter X-ray waves, primarily through the atoms' electrons. When an X-ray (electromagnetic wave) strikes an electron, secondary spherical waves will emanate from the electron. This phenomenon is known as elastic scattering, and the electron is known as the scatterer. A regular array of scatterers will produce a regular array of spherical waves. Although these waves cancel one another out in most directions through destructive interference, they add constructively in a few specific directions, which are determined by Bragg's law:

$$n\lambda=2d\cdot\sin\theta \quad (1)$$

Where d is the spacing between diffracting planes, θ is the incident angle, n is any integer, and λ is the wavelength of the beam. These spherical waves will be in synchrony only in directions where their additional path length equals to an integer multiple of wavelength, producing a reflection spot in the diffraction pattern. X-rays are used to produce the diffraction pattern

because their wavelength λ is typically the same order of magnitude (1-100 Å) as the spacing d between planes in the crystal.

2.3.6 Energy Dispersive X-ray Spectroscopy

Energy-dispersive X-ray spectroscopy (EDS or EDX) is an effective analytical technique that can be used for the elemental or chemical characterization of a sample. The EDX spectrum can be obtained through the interaction of some source of X-ray excitation and a sample. Its characterization capabilities are due in large part to the fundamental principle that each element has a unique atomic structure, which allows unique series of peaks on its X-ray spectrum, which is shown in Figure 2-4. To obtain the emission of characteristic X-rays from a specimen, a high-energy beam of charged particles such as electrons or protons, or a beam of X-rays, is focused and hit onto the sample being studied. An atom within the sample contains ground state (or unexcited) electrons in discrete energy levels (electron shells) bound to the nucleus. The incident high-energy beam may excite an electron in an inner shell, ejecting it from the shell while creating an electron hole where the electron was. An electron from an outer, higher-energy shell then fills the hole, and the difference in energy between the higher-energy shell and the lower-energy shell may be released in the form of an X-ray. The number and energy of the X-rays emitted from a specimen can be measured by an energy-dispersive spectrometer. As the energy of the X-rays is characteristic of the difference in energy between the two shells, and of the atomic structure of the element from which they were emitted, this allows the elemental composition of the specimen to be measured.

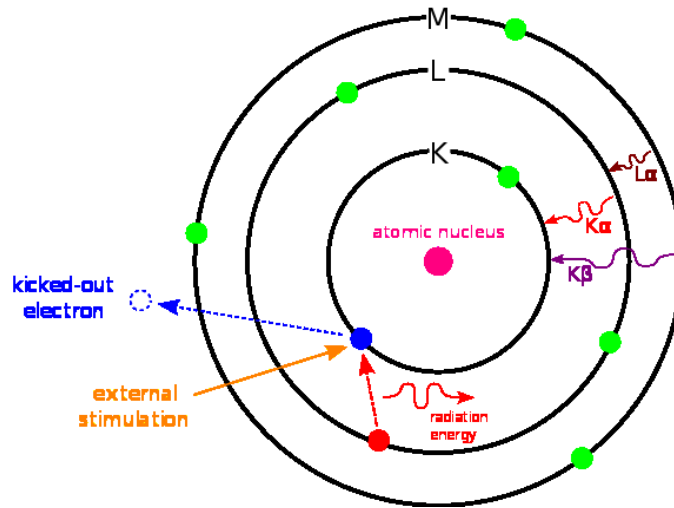


Figure 2-4 Principle of X-ray generation.

2.3.7 PID Controller

A proportional–integral–derivative (PID) controller is a general loop feedback controller and widely used for industrial control systems. A PID controller calculates an "error" value as the difference between a measured process variable and a desired setpoint. The controller attempts to minimize the error by adjusting the process control inputs. The PID controller algorithm contains three separate parameters: the proportional (P), the integral (I) and derivative (D) values. These values can be interpreted in terms of time: P depends on the present error, I on the accumulation of past errors, and D is a prediction of future errors, based on current rate of change. The weighted sum of these three actions is used to adjust the process via a control element such as the position of a control valve, or the power supplied to a heating element. Beside the use of PID controllers, some applications may require using only one or two

parameters to provide the appropriate system control. This is achieved by setting the other parameters to zero. A PID controller will be called a PI, PD, P or I controller in the absence of the respective control actions.

2.3.8 Portable Miniature Spectrometer

A miniature fiber-optic spectrometer, USB4000, has been used for various optical and spectral sensing tasks with high-performance. The new improved design includes an advanced detector array and powerful high speed electronics. The detector array is a 3648 pixel array for excellent spectral resolution and the electronic provide a 300:1 signal to noise ratio. There is a 16 bit A/D, four triggering options, a dark current correction feature and a 22 pin connector. Also, with the operational software (SpectraSoft), USB4000 can be operated with computer, which have Windows, Linux or Mac operation system, by connecting via the USB port and it will draw power from the host computer without the need for an external power supply. USB4000 is responsive from 200-1000nm, but the specific range depends on the grating and entrance slit selections.

How light moves through the optical bench of an USB4000 spectrometer can be understood by referring to its cut-away diagram, which is shown in Figure 2-5. 1 is where a fiber input line brings the signal into the spectrometer; 2 is the entrance slit whose size can be specified; 3 is an optional filter; 4 is the collimating mirror; 5 is the grating, where wavelength range can be factory adjusted; 6 is the focusing mirror; 7 is where an optional detector collection lens may be installed; 8 is the detector array; 9 is the order sorting filter (if used); 10 is an

upgrade to extend the detector response into the UV. All of these parts combine to make a highly effective spectrometer.

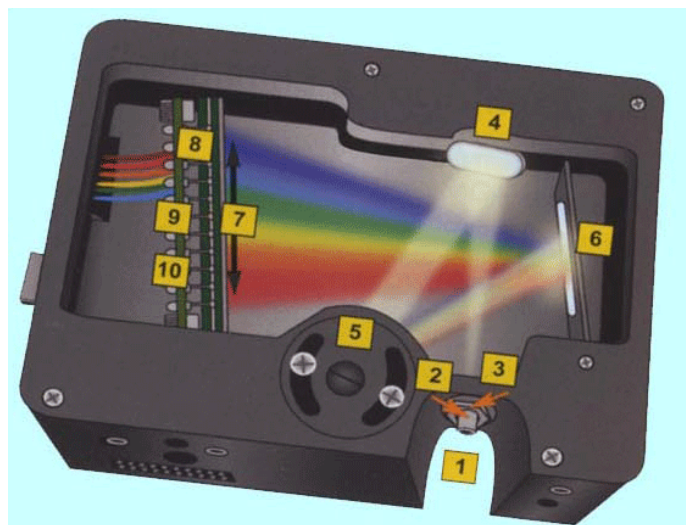


Figure 2-5 A cut-away diagram of an USB4000 spectrometer.

2.4 Experimental Section

2.4.1 Template Preparation

Glass microscope or quartz slides are cut into 25mm-diameter disks and cleaned at 80°C for 30 min in a piranha solution that contains 3:1 concentrated H_2SO_4 : 30% H_2O_2 , and rinsed repeatedly using deionized water (resistivity 18.2 M Ω) until the pH value of the solution reaches 6. This cleaning removes organic contaminants from slides. The slides are then sonicated in 5:1:1 $\text{H}_2\text{O}:\text{NH}_4\text{OH}:\text{H}_2\text{O}_2$ solution for 60 min, and washed with a large amount of water until the pH value reaches 6 again. After such treatment, the slides become very hydrophilic due to the

production of hydroxyl groups. The prepared slides are stored in deionized water and used within one week. In order to form nanosphere mask, $\sim 2.5 \mu\text{l}$ of the nanosphere solution at its original concentration is dropped onto a cleaned glass slide that has a thin water film. The existence of such film can facilitate the diffusion of nanospheres over the glass substrate and prevent the fast drying of the suspension. Then the slide is stored inside a covered Petri dish to allow the slow evaporation of water, which is helpful to form a closely packed monolayer of nanospheres.

2.4.2 Preparation of Periodic Gold Nanoparticle Arrays

After making the nanosphere monolayer, an ordered array of nanoparticles are produced by depositing metals onto the interstitial spaces between the closely packed nanospheres. A thermal evaporator (Denton) is used to deposit 2nm chromium and then 48nm gold on glass slides in vacuum (10^{-6}Pa). The thicknesses of the films are monitored by quartz crystal microbalance. After taking samples out the evaporator, the nanospheres are removed by sonicating samples in absolute ethanol for 3 min. The whole procedure is shown in Figure 2-6. The gold nanoparticles are strongly attached to the glass slides by the adhesive chromium layer. After that, the gold nanoparticle coated slides are annealing at different temperature for certain time.

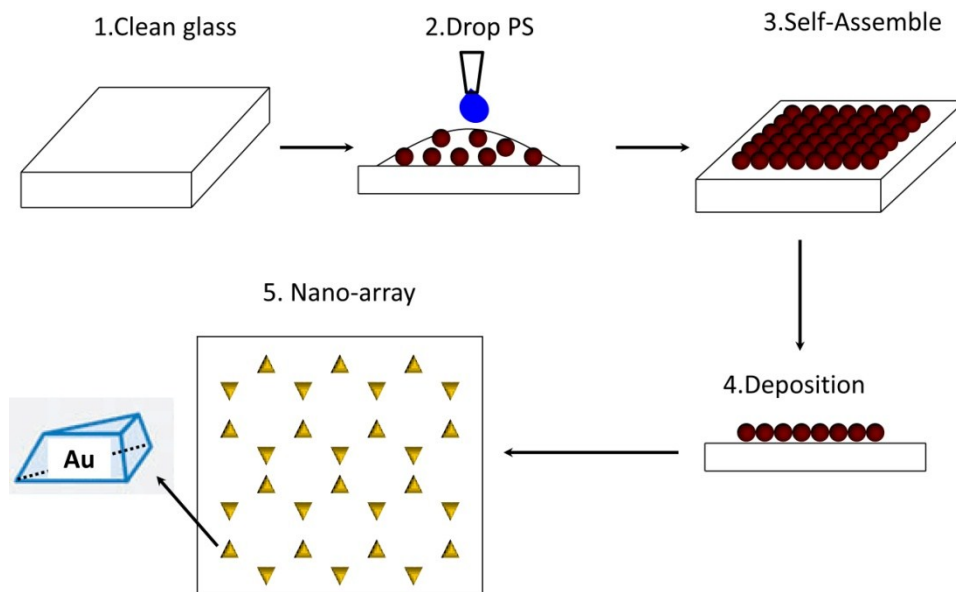


Figure 2-6 Schematic of gold nanoparticle arrays fabrication process.

2.2.3 Deposition of Polyelectrolyte Multilayer Films

The chemical structure for poly (acrylic acid) (PAA) and poly (allylamine hydrochloride) (PAH) is depicted in Figure 2-7. Both polymers have chains approaching micrometers scale in length depending on intended use (e.g. a representative molecular weight of approximately 50,000 amu for PAH representing approximately 1,000 monomers, for a length on the order of 0.25 μm). The layer-by-layer (LBL) assembly of oppositely charged polyelectrolytes is facilitated by the formation of water-insoluble complexes of polycations and polyanions via the electrostatic attractions between the carboxylate (COO^-) and ammonium (NH_3^+) groups. This interaction is well-established for the layer-by-layer deposition of polyelectrolyte multilayers by alternating oppositely charged polyelectrolytes.

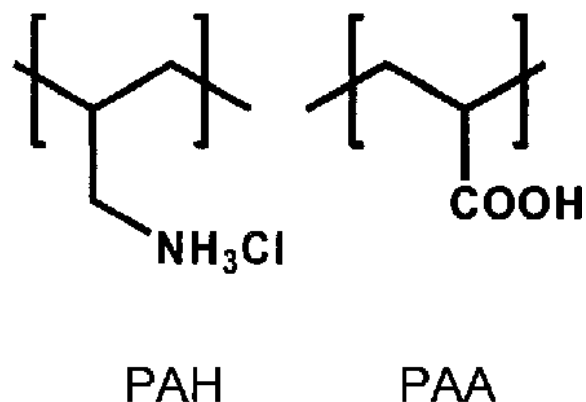


Figure 2-7 Chemical structure of poly (allylamine hydrochloride) (PAH) and poly (acrylic acid) (PAA).

Polyelectrolyte multilayers are deposited on the nanoparticle arrays through layer-by-layer (LBL) method and the process is shown in Figure 2-8. The multilayers are deposited from 0.01 M solutions of PAA and PAH at pH of 3.5 and 8.5, respectively. The deposition involves the immersion of charged surfaces (i.e. glass) into the aqueous solutions of both polyanions and polycations in an alternating sequence to build multilayers by electrostatic interaction. Briefly, the glass slides are immersed in the PAH solution for 15 minutes, and rinsed with DI water for three times in separate beakers. The slides are then immersed in the PAA solution for 15 minutes and rinsed with DI water for three times as well. Such deposition cycle is repeated for n times to deposit n bilayers of PAH and PAA. Either PAA or PAH layer can be used as the ending layer. For example, (PAH/PAA) $_3$ means three bilayers of PAH/PAA, where PAA is the ending layer; (PAH/PAA) $_3$ -PAH means three bilayers of PAH/PAA and an additional PAH is the ending layer.

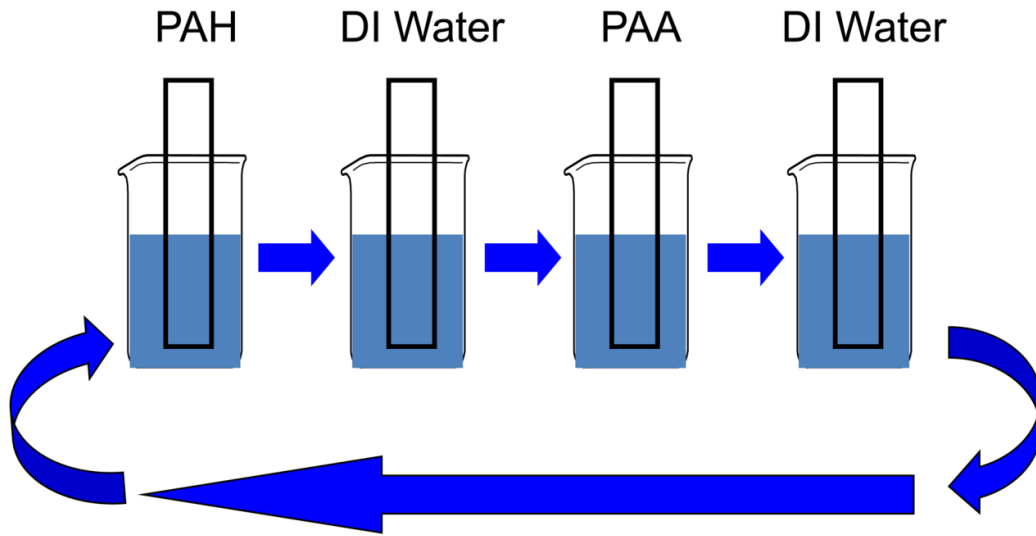


Figure 2-8 Layer-by-layer deposition of PAH and PAA multilayers.

2.2.4 Fabrication of Pattern Using Photolithography

The glass substrates with nanoparticle arrays are washed with ethanol and then dried at air. In order to make the pattern on the substrates, a droplet of the photoresist AZ4620 is firstly dropped in the center of the substrate. The substrate is then spun at 500rpm for 6sec and then spun at 3000rpm for 40sec. After that, the substrate is allowed to settle for 2 min on the spin stage and then carefully moved the substrate to a flat and room temperature surface. Secondly, the photoresist coated substrates are put on a hot plate to bake at 95°C for 5min. Thirdly, the soft baked substrates are exposed to UV light for 10min after aligning the photomask. Finally, the substrates are developing in a developer solution of AZ400K with the ratio of 1:3 AZ400K to water for 1min. The developed substrates are rinsed with distilled water, blow dried with nitrogen and ready to use.

2.2.5 Experimental Setup

The custom-made localized surface plasmon resonance measurement system contains six essential components: light source, optical fiber, optical measurement cell, temperature controlling system, USB4000 spectrometer and data collection system. The whole experimental set-up is shown in Figure 2-9.

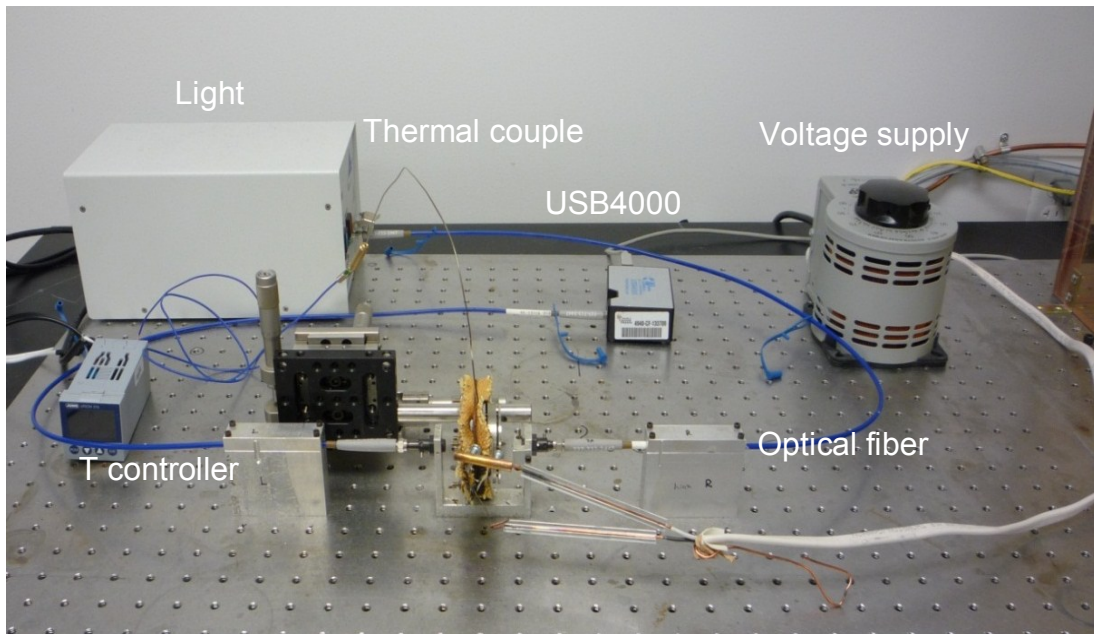


Figure 2-9 Experimental set-up.

The deuterium tungsten halogen light source (DH-2000) is used as the illumination source. It combines the continuous spectrum of deuterium and tungsten halogen light sources in a single optical path, which produces produces a powerful, stable output from 215-2000 nm.

The optical fibers with diameter of 600 μ m are used for conveying the incident light and transmitted light. The standard unjacketed fiber consists of three layers. The innermost layer is a pure, fused-silica core that is surrounded by a doped fused-silica cladding. This core/clad composite of unprotected fiber is fragile. In order to improve its strength, it is triple-coated with a polyimide buffer during the drawing process. Finally, to reduce stray light and strengthen the fiber, it is applied a special material coating.

A sample of glass substrate with gold nanoparticle arrays is fixed onto the self-built measurement chamber. One side of the cell is transparent glass and another side is the fixed sample. The cell has an inlet and outlet to allow the liquid or gas to pass through the chamber continuously. The light is incident on the sample perpendicularly through the optical fiber and the transmitted light is collected and transferred to the computer by a portable miniature spectrometer.

A resistive heating wire, which is made of a nickel-chromium alloy, coupled to the proportional-integration-differentiation (PID) controller (JUMO, Germany) is used to heat or cool the measurement cell with a pre-designed program. A thermocouple is placed close to the sample to measure its temperature. The power to the resistor is supplied by a DC power supply.

The USB4000 miniature fiber optic spectrometer, responsive from 200-1100nm, is used to collect the optical signals. Data programmed into a memory chip on each USB4000 includes wavelength calibration coefficients, linearity coefficients, and the serial number unique to each spectrometer. The spectrometer operating software reads these values from the spectrometer after connecting to a computer via the USB port. The USB4000, like all USB devices, can be

controlled by commercial software (SpectraSuite, Ocean Optic), which is installed and operated on Windows, Linux or Mac operating systems.

All spectra are collected in transmission mode with SpectraSuite software using normally incident non-polarized white light with beam size of about 2 mm^2 , which can be adjusted by an optical aperture. Each spectrum is an average of 25 individual ones at 8 ms integrations, and the collection is performed in either a gas or liquid environment.

CHAPTER 3: FABRICATION AND CHARACTERIZATION OF HIGHLY STALBE GOLD NANOPARTICLE ARRAYS

3.1 Introduction

In the chapter, I report study of a quality of polystyrene nanospheres monolayer formed on substrates; then, I describe the preparation and characterize gold nanoparticle arrays formed on glass and quartz substrates. Finally, I discuss the temperature effects on the extinction spectra of gold nanoparticle arrays.

3.2 Results and Discussion

3.2.1 Quality Control of Polystyrene Nanosphere Monolayer

Nanosphere lithography is an inexpensive, material specific and high-yield method of making nanostructures, and can be used to make arrays of metallic nanoparticles with precisely controlled size and interparticle spacing. In this method, nanospheres are close-packed on a substrate to form an ordered hexagonal array, followed by the deposition of a thin film of metal. After removing the spheres, the remaining 2D array of metal on the substrate consists of triangular shaped nanostructures in a hexagonal pattern. Polystyrene nanospheres with diameter of 390 nm are used as deposition mask. Figure 3-1 is a typical optical microscopic image of self-assembled polystyrene nanosphere layers on a glass substrate, where three different typical areas (1, 2 and 3) with different color can be seen clearly. The packing of the nanospheres in the

different colored areas are characterized by SEM. Figure 3-2A shows an optical image of green colored area. The SEM image shows that polystyrene nanospheres are close-packed (Figure 3-2B), where most of nanospheres are close to each other and packed well. Figure 3-3A shows the optical image of an area with a light green color. SEM image shows that nanospheres are packed multilayers at this area (Figure 3-3B). Figure 3-4A shows the optical image of an area with a blue color. SEM image shows that nanospheres are under packed (Figure 3-4) with clear spacing between different nanospheres.

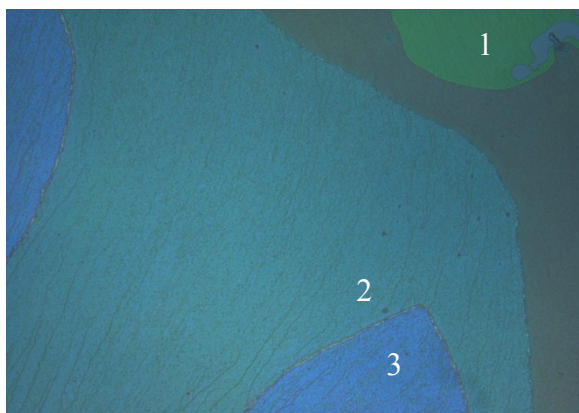


Figure 3-1 A typical optical microscopic image of self-assembled polystyrene nanosphere on the clean glass surface with different configuration: (1) monolayer; (2) multilayers; (3) under-packed monolayer.

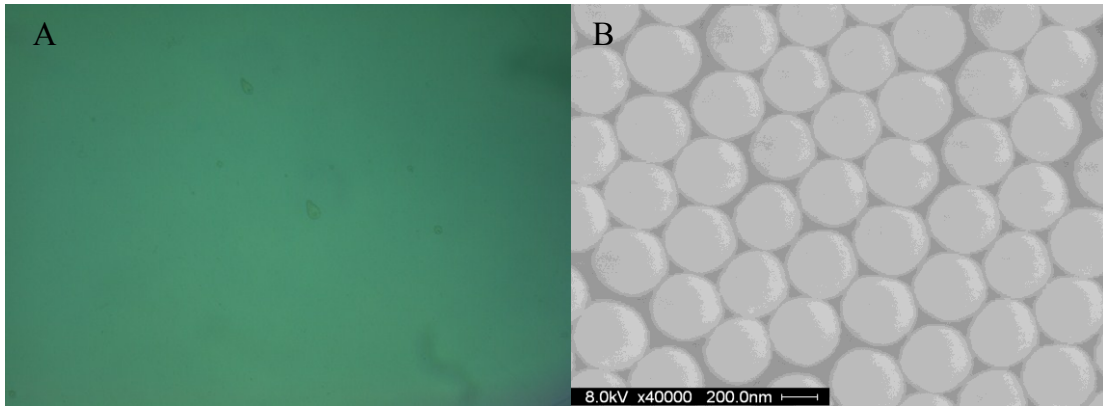


Figure 3-2 An optical microscopic image of self-assembled close-packed polystyrene nanosphere monolayer (A); SEM image of polystyrene nanosphere monolayer (B).

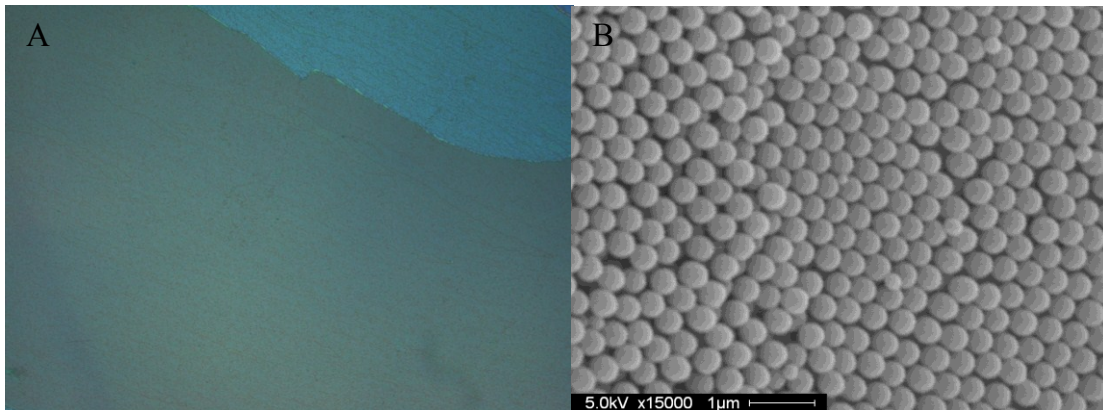


Figure 3-3 An optical microscopic image of self-assembled polystyrene nanosphere multilayer(A); SEM image of polystyrene nanosphere multilayer (B).

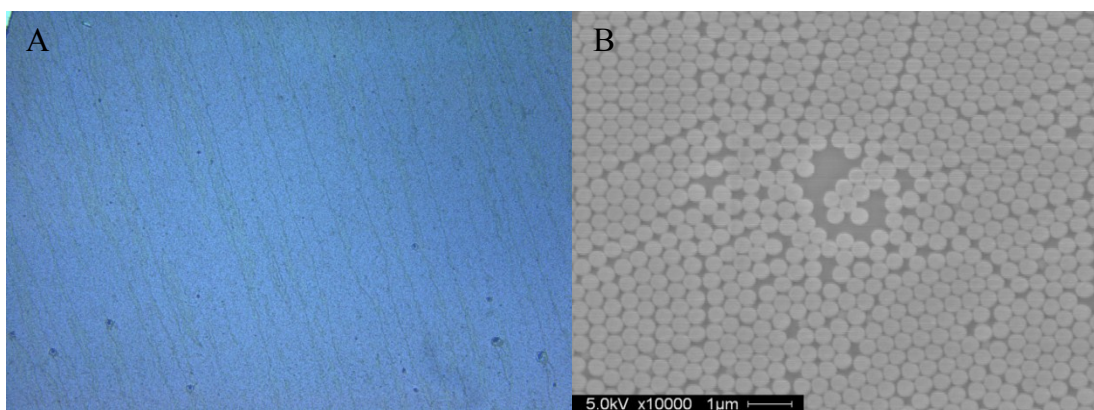


Figure 3-4 An optical microscopic image of self-assembled under-packed polystyrene nanosphere monolayer(A); SEM image of polystyrene nanosphere multilayer (B).

Nanosphere monolayers on solid substrates show strong color when illuminated with light. Both diffraction and interference contributes to the color of nanosphere layer. The characteristic color of monolayers depends on the type of materials, nanosphere size, lattice orientation, and interparticle spacing. For close-packed nanospheres monolayers, the size of the nanospheres leads to two distinct colors. First, ordered nanosphere monolayers with diameter over 500 nm exhibit strong iridescence, which mainly depends on illumination and observation angles. This phenomenon is due to diffraction of light in layered arrangement of nanospheres as in butterfly wings.⁸³ Light scattered by individual nanosphere will interfere with that scattered from neighboring ones, and give rise to amplification (constructive interference) or annihilation (destructive interference) of light at certain wavelengths.⁸⁴ Second, ordered nanosphere monolayers with size below 500 nm show a continuous and uniform color. This color is a result of interference of light at the parallel planes of the monolayer surface and the substrate.⁸⁵ The uniform coloration strongly depends on the size of the nanospheres and their construction

structures. This is useful for quality control of monolayers, where electron microscopy is time consuming and cumbersome.

Treating the closed-packed monolayer as a continuous, plane parallel film, one can apply classical optics to describe the interference between the light reflected at the surface of the thin film and the supporting substrate.⁸⁶ The intensity of reflected light depends on the optical path difference between the electromagnetic waves reflected at the air–nanosphere and the nanosphere–substrate interfaces. When illumination occur normal to the surface, interference of two parallel light beams (beam 1 and beam 2) occurs, which is schematically depicted in Figure 3-5. The closed-packed nanosphere monolayer is approximated as a continuous thin film with a thickness d_{coll} and an effective refractive index n_{mono} . The additional optical path length Δ that the light of beam 2 travels compared to beam 1 equals $\Delta = 2d \cdot n_{mono}$, and constructive interference occurs for integral multiples of the wavelength ($m\lambda$, $m=1, 2, \dots$) of the incident beam. Hence, it follows that the wavelengths that are constructively reflected can be determined by

$$m\lambda = 2d_{coll}n_{mono} \quad (m = 1, 2, \dots) \quad (1)$$

In the equation (1), λ represents wavelength of maximum reflection, d_{coll} is the diameter of nanospheres, and n_{mono} is the refractive index of nanosphere monolayer.

The refractive index of the monolayer, n_{mono} , depends on the refractive index of polymer material (polystyrene), n_{PS} , the volume fraction of nanospheres, φ_{coll} , and the refractive index of the surrounding medium (air), n_{med} , and can be expressed as⁸⁷

$$n_{mono} = n_{PS}\varphi_{coll} + n_{med}(1 - \varphi_{coll}) \quad (2)$$

Substituting Equation (2) into (1) and taking $n_{med}=1$ for air as surrounding medium, an expression for the reflection maxima is obtained:

$$\lambda = \frac{2}{m} d_{coll} [n_{PS} \varphi_{coll} + (1 - \varphi_{coll})] \quad (3)$$

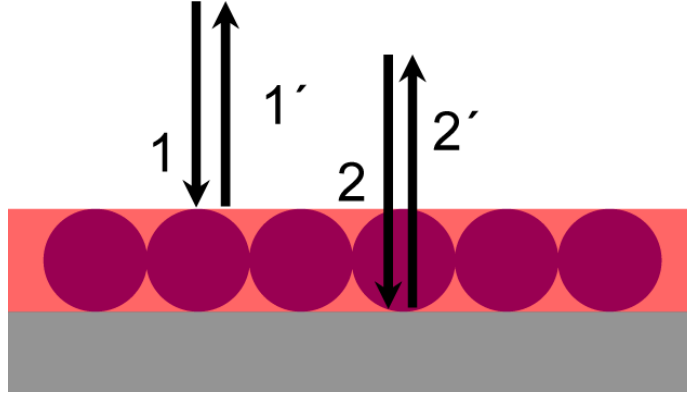


Figure 3-5 Interference between light beams reflected at the air-monolayer and monolayer-substrate plane.

The volume fraction of the colloids in a close-packed monolayer is derived by using a theoretical model, which is shown in Figure 3-6. Using geometric arguments, the volume fraction can be approximated as the volume fraction of a sphere with the diameter d_{ncp} (being the diameter of the colloid in the non-close packed monolayer) in a hexagonal prism with the base determined by d_0 (d_0 being the initial diameter of the spheres in the close-packed arrangement). To derive the formula for the volume fraction, we can start with the prisms. The area of the prism base can be described as 6 interconnected equilateral triangles with a height of $d_0/2$; the height of the prism is d_0 , so the volume of the prism is

$$V_{prism} = A_{Base} \cdot d_0 = \frac{3}{2\sqrt{3}} \cdot d_0^3 \quad (4)$$

The volume fraction φ_{coll} can now be expressed as follows:

$$\varphi_{coll} = \frac{V_{coll}}{V_{prism}} = \frac{\pi\sqrt{3}}{9} = 0.604 \quad (5)$$

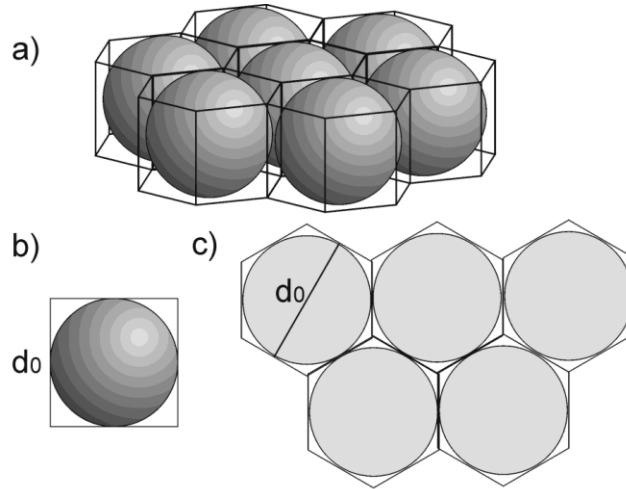


Figure 3-6 Theoretical calculation of the volume fraction of close-packed nanospheres monolayer treated as a continuous thin film and the complete film is modeled as an array of interconnected hexagonal prisms with the base d_0 (a); the height of the prisms equals the nanosphere diameter d_0 ; the base of the prism equals the diameter of nanospheres (c).

In this research, the diameter of polystyrene nanosphere is 390nm and the refractive index is 1.57, where the wavelength dependence was neglected. Putting all of these parameters into equation (3), the calculated first and second order maximum of absorption peak are 1049nm and 524nm, respectively. Figure 3-7 shows the ultraviolet-visible (UV-Vis) extinction spectra of a polystyrene nanospheres monolayer on glass substrate, where the second order maximum of observed absorption peaks is 500nm, and the first order absorption peak is out of the detection range of our spectrometer. It shows that a qualitative agreement between theoretical and experimental data is obvious. The difference between second ($m=2$) interference maxima of theoretical and experimental data are explained by oversimplification of the model, where the order of monolayer is assumed to be perfect and defects are neglected. In reality, the packing of

nanospheres monolayer is not perfect. Thus, the volume fraction of the colloids is overestimated in the model.

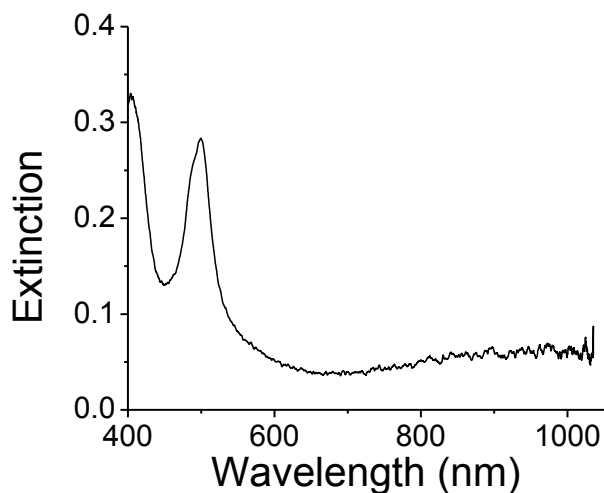


Figure 3-7 UV-Vis extinction spectrum of a polystyrene nanospheres monolayer on the glass substrate.

3.2.2 Capillary Force Between Colloidal Particles

In the fabrication process, an ordered polystyrene nanosphere monolayer is used as the evaporation mask for the preparation of periodic arrays of metal nanoparticles. In order to understand the mechanism of the hexagonal ordering, the role of capillary forces must be considered due to the fact that they play an essential role in the two dimensional (2D) aggregation and ordering of nanoparticles. Capillary forces are defined as the interaction between nanosphere and solution interfaces. To distinguish the capillary forces of floating

nanospheres from the one of partially immersed nanospheres in a liquid phase, the former and latter are called lateral flotation forces and lateral immersion forces, respectively. The origin of lateral capillary forces is the deformation of the liquid interface, also called menisci, produced by each individual nanosphere.⁸⁸⁻⁹⁰

The mechanism of 2D nanosphere arrays influenced by the lateral capillary forces that present in my case have been intensively studied and a two-step process for self-assembly of the nanospheres is identified.⁹¹ In the first step, the solvent (usually water) starts to evaporate and when the thickness of the solvent film becomes almost equal to the diameter of nanospheres, a nucleus consisting of some nanospheres sticking on the substrate is produced. In the second step, the cluster starts to grow, because evaporation of the solvent caused a permanent flux of nanospheres which flows toward the nucleus, gets trapped and forms an ordered array. This is exactly what happens in my experiment. When a droplet of aqueous polystyrene nanospheres solution deposits onto the substrate, the water film begins to evaporate and then a nucleus is formed. Driven by the flux of nanospheres, the ordering process of nanospheres is carried out to form a close-packed monolayer.

3.2.3 Geometry Calculation of Nanoparticles

The fabricated nanoparticles size and interparticle distance can be calculated geometrically according to the size of nanospheres. Figure 3-8A shows a schematic illustration of a close-packed polystyrene nanosphere monolayer mask that was used for metal evaporation. When doing the metal deposition using a thermal or e-beam evaporation method, the metal vapor

will come into the space between the close-packed nanospheres monolayer. After removing the mask, the periodic metallic nanoparticle arrays will be left on the deposition substrate. Figure 3-8B shows the geometry calculation of particle size and interparticle distance. The length of GI is defined as the in-plane particle size and the length of CK as the interparticle distance. Supposing the diameter of the polystyrene nanosphere is D , according to the geometry relationship, the GI (in-plane particles size) is equal to $(\sqrt{3}-3/2)D$ and CK (interparticle distance) is $(1/\sqrt{3})D$. The diameter of the polystyrene nanosphere I used is about 390 nm, so the theoretical calculated particle size and interparticle distance is 90 nm and 225 nm, respectively.

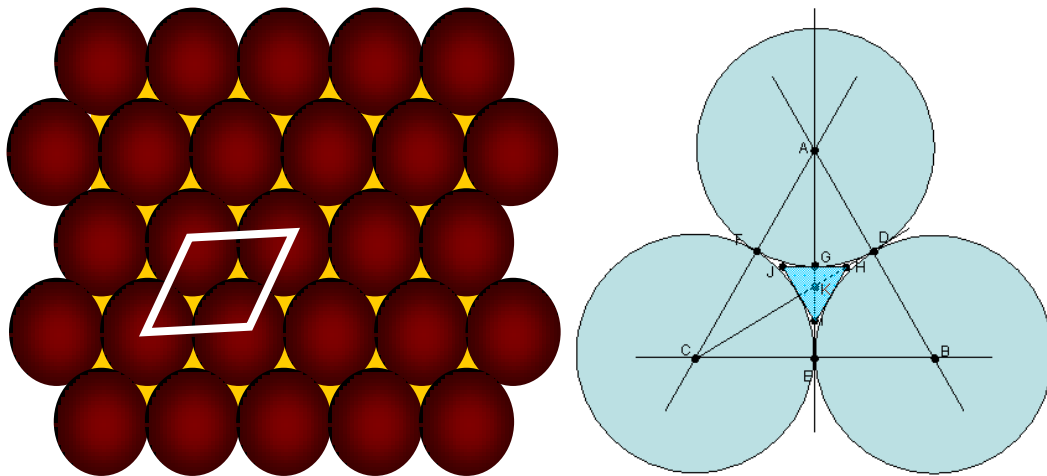


Figure 3-8 Schematic illustration of closed-packed polystyrene nanosphere monolayer mask (A); geometry calculation of metallic nanoparticle size (B).

3.2.4 Gold Nanoparticle Arrays on Glass

3.2.4.1 AFM Characterization

An atomic force microscope (AFM) has been used to image the two dimensional periodic arrays of gold nanoparticles deposited on the borosilicate glass slide. Figure 3-9 shows that deposited nanoparticles are arranged into hexagonal patterns after the polystyrene nanospheres are removed. Although some nanoparticles connect each other to form a chain, such long chain structure has optical response in far infrared region, thus will not affect measurements in visible wavelength region. Those defect sites are caused by packing imperfections in the polystyrene nanospheres monolayer mask.

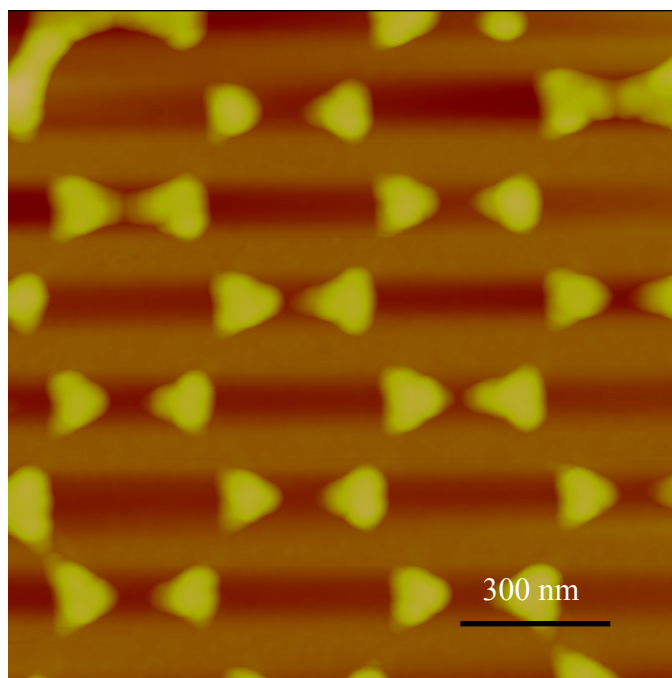


Figure 3-9 AFM images of gold nanoparticle arrays on the glass substrate.

Figure 3-10 is a high resolution AFM image of gold nanoparticles. It shows that the “as-deposited” nanoparticles have triangular in-plane shapes. And the AFM analysis results shows that the average diameter and interparticle distance are ~ 100 and 225 nm, respectively. The heights of nanoparticles measured from cross sections are 50 nm. The value of triangular particle size measured by AFM is larger than that from theoretical calculated value (90 nm). Also the tips of the nanoparticles are looking more round in the AFM images. These differences can be explained by the fact that the AFM values have not been corrected for tip broadening effects.

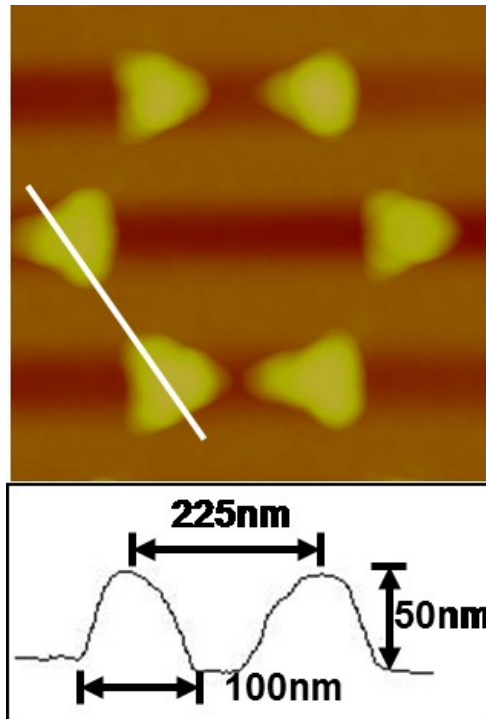


Figure 3-10 AFM analysis of gold nanoparticles.

3.2.4.2 Temperature-induced Shape Changes

The final shape of gold nanoparticles after annealing is dependent on the annealing temperature and the annealing time. Figure 3-11 shows a close-up AFM image of annealed gold nanoparticle arrays after thermal annealing at 300°C for 1 hour. The profile of the triangular nanodisks before thermal annealing is clearly visible in this figure. The facets of the nanoparticle correspond to the apexes of the triangular nanodisks prior to thermal annealing. In my experiment, an annealing temperature (300°C) is used that is lower than the melting point of bulk gold (1063°C). However, the annealing temperatures were sufficiently high to cause surface melting of the gold nanoparticles at the apexes of the triangular nanodisks. As a result, the surface tension of the melted gold material caused the “retraction” of these softened apexes to form the observed more rounded shape. It should be noted that for nanoscale materials their melting point is expected to be lower than the melting point of the corresponding bulk material if the particle is very small. Thus we were able to cause shape transformation of these triangular nanodisks despite the fact that the annealing temperatures employed were comparatively lower than the bulk melting temperature. When the annealing is sufficiently high, the surface melting of gold nanoparticles will become more strenuous or even melting of whole nanoparticles. Figure 3-12 shows an AFM image of gold nanoparticles arrays that after annealing at 600°C for 1h, the triangular shaped gold nanoparticles were transformed to spherical nanoparticles. The reason for this is because the spherical nanoparticles have the lowest surface energy at equilibrium if the whole volume is constant.

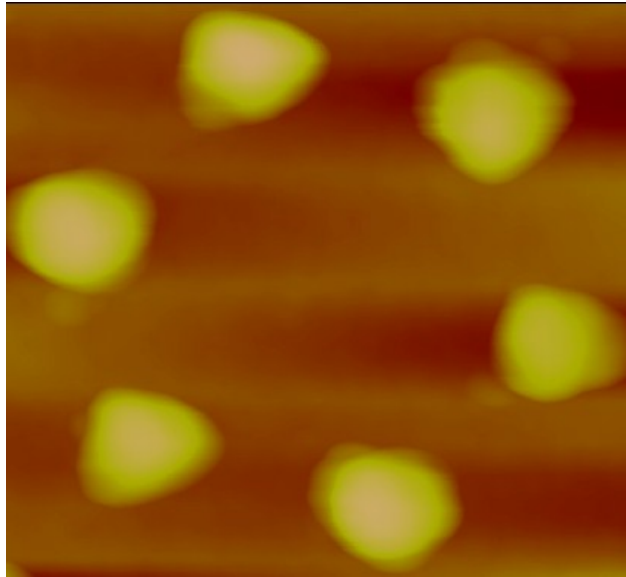


Figure 3-11 AFM image of gold nanoparticles after polystyrene nanospheres removed and annealed at 300°C for 1 hour.

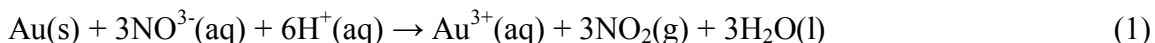


Figure 3-12 AFM image of gold nanoparticles after polystyrene nanospheres removed and annealed at 600°C for 1 hour.

3.2.4.3 Confirmation of Nanoparticle Size and Shape

Aqua regia (English: 'royal water') or aqua regis ('king's water') is a highly corrosive mixture of acids, fuming yellow or red solution also called nitro-hydrochloric acid. The mixture is formed by freshly mixing concentrated nitric acid and hydrochloric acid, usually in a volume ratio of 1:3, respectively. It was named so because it can dissolve the so-called royal metals or noble metals, gold and platinum, which single acids alone cannot do. However, ruthenium, tantalum, iridium, osmium, titanium, rhodium and a few other metals are capable of withstanding its corrosive properties.

Aqua regia dissolves gold. Although neither constituent acid will do so alone because in combination each acid performs a different function. Nitric acid is a powerful oxidizer, which will actually dissolve a virtually undetectable amount of gold forming gold ions (Au^{3+}). The hydrochloric acid provides a ready supply of chloride ions (Cl^-), which react with the gold ions to produce chloroaurate anions also in solution. The reaction with hydrochloric acid is an equilibrium reaction which favors formation of chloroaurate anions (AuCl_4^-). This results in a removal of gold ions from solution and allows further oxidation of gold to take place. The gold dissolves to become chloroauric acid. In addition, gold may be dissolved by the free chlorine present in aqua regia. Appropriate reaction equations are:



Since annealing temperature is close to the softening temperature of the Pyrex glass ($\sim 750^\circ\text{C}$), the annealing process produces semi-embedded nanoparticles. In order to see whether

the gold nanoparticles are sitting on the substrate surface or embedded in the glass and to determine the real shape and size of the nanoparticles, the gold nanoparticles are removed by etching in an aqua regia solution for 20 min. Figure 3-13 shows the AFM image of nanohole arrays on the glass substrates after etching off the gold nanoparticles arrays. The AFM measurement shows the size and depth of the hole is 50nm and 25nm, respectively. These results confirm the gold nanoparticles are spherical shape and around half of the nanoparticles are embedded in the glass substrate.

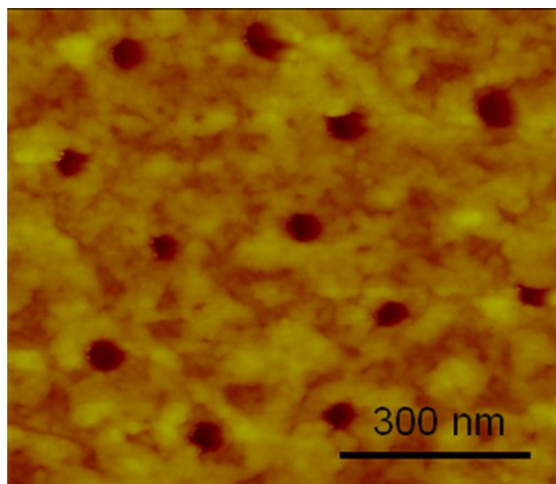


Figure 3-13 AFM images of nanohole arrays on the glass substrate after etching off annealed gold nanoparticle arrays.

3.2.4.4 Shape Effect on LSPR

As mentioned before, the LSPR of metallic nanoparticles are also dependent on their size and shape. As shown in Figure 3-14, a strong LSPR peak at 780 nm and a less intense peak at 560 are observed in the optical extinction spectrum of the fabricated triangular gold nanoparticle arrays. These peaks can be attributed to the excitation of a quadrupolar and dipolar LSPR. This is

accordance with theoretical calculations presented from different groups using the discrete dipole approximation (DDA) method. However, the peak at 560 nm can be precisely explained as an overlap between the quadrupolar LSPR of the triangular particles. Below 500 nm the absorption increases due to the interband transition, i.e. the transition of electrons from the Au 5d band to empty 6sp bands above the Fermi level. The optical spectra of the triangular NPs after preparation followed perfectly the theoretical calculations reported by Shuford et al.⁹² For the annealed sample, half of the particle is embedded in a glass matrix as mentioned before. The extinction spectrum shows that only one resonance peak at around 560 nm is observed while the LSPR peak at 780 nm disappears. The optical changes can be explained by shape transformation of gold nanoparticles from triangular to spherical.

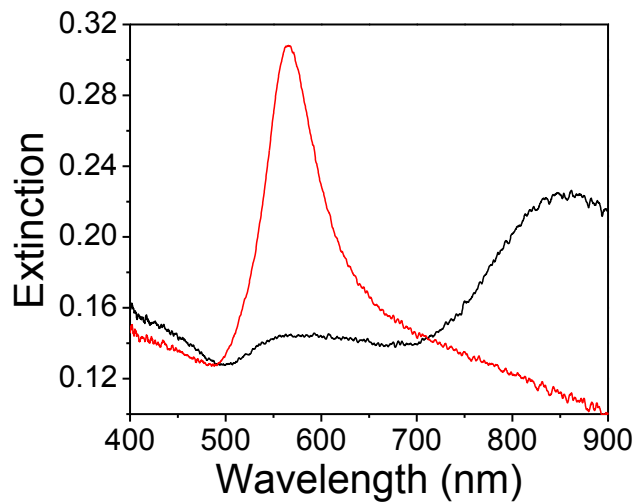


Figure 3-14 Extinction spectra of gold nanoparticle arrays on the glass substrate before (black curve) and after (red curve) annealing.

3.2.4.5 Thermal-induced LSPR Peak Shift

The temperature effects on the peak shifts have been calibrated. Increasing temperature at a heating rate of 5°C/min leads to the LSPR peak shifts of annealed gold nanoparticles to long wavelength and the corresponding extinction spectra are shown in Figure 3-15. Figure 3-16 shows the LSPR peak shift versus the temperature. The temperature dependent shift can be understood from the dispersion relation for surface plasmon waves, together with the decrease in plasmon frequency and increase in collision frequency in the Drude model as the temperature increases. The LSPR peak returns to its original position after the sample is cooled down to room temperature. The processes of the heating-cooling cycle can be repeated many times. The magnitude of peak shifts is linearly proportional to temperature between 20 and 300 °C. Such linear response is the result of structural stability of annealed gold nanoparticles. The details of the discussion are as follows.

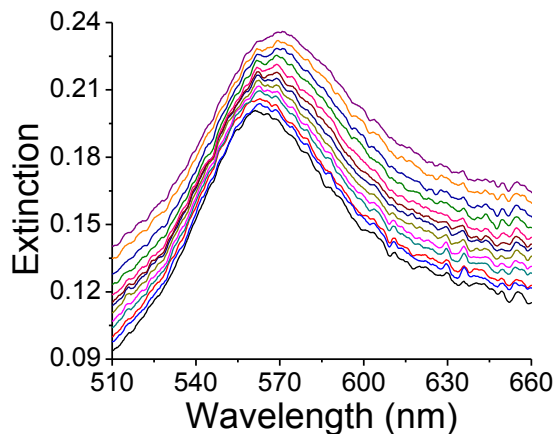


Figure 3-15 Extinction spectra of thermally annealed gold nanoparticle arrays on the glass substrate at different temperature from 30-300 °C (bottom to up).

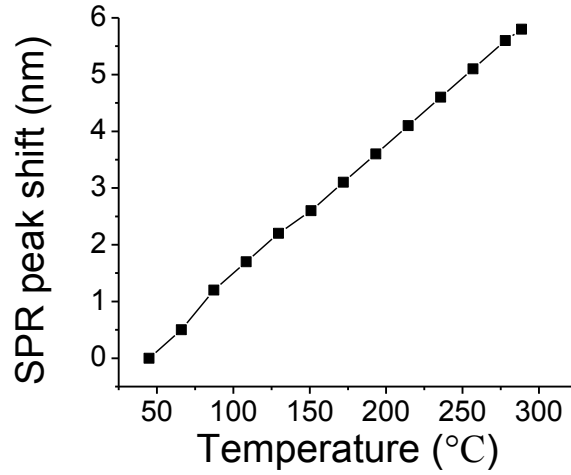


Figure 3-16 LSPR peak shift versus the temperature.

In order to understand my experimental results, we have adopted a semi-empirical model for the temperature dependence of the surface plasmon excitation. For the isolated gold nanoparticle, we adopted already established temperature-dependent Drude model in which both the plasmon and collision frequencies vary with the temperature: the former through a simple volumetric effect, and the latter through its dependence on the electron-phonon and electron-electron collisions, respectively.⁹³ A brief summary of the proposed model is shown as follows.

According to the Drude model, the metal dielectric functions as follows:

$$\varepsilon = 1 - \frac{\omega_p^2}{\omega(1+i\omega_c)} \quad (1)$$

Where ω_c is the collision frequency and ω_p is the plasma frequency, which is given by the following equation:

$$\omega_p = \sqrt{\frac{4\pi N e^2}{m^*}} \quad (2)$$

Where N and m^* are density and effective mass of the electrons. The collision frequency will have contributions from both phonon-electron and electron-electron scattering, which is the sum of phonon-electron and electron-electron scattering:

$$\omega_c = \omega_{cp} + \omega_{ce} \quad (3)$$

For surface plasmon resonance (SPR), one must account for the temperature (T) variation on ω_p besides that for ω_c . ω_p will depend on T via volumetric effects as follows:

$$\omega_p = \omega_{p0}[1 + \gamma(T - T_0)] \omega_{p0}[1 + \gamma(T - T_0)]^{-1/2} \quad (4)$$

Where γ is the expansion coefficient, T_0 is a reference temperature (room temperature).

$$\omega_{cp}(T) = \omega_0 \left[\frac{2}{5} + 4 \left(\frac{T}{\theta} \right)^5 \int_0^{\theta/T} \frac{z^4 dz}{e^z - 1} \right] \quad (5)$$

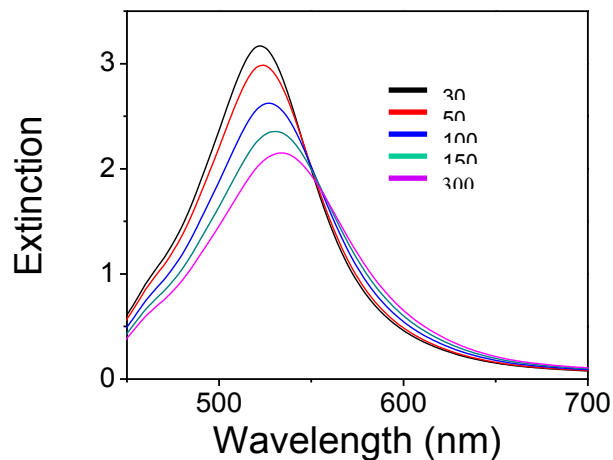
Where θ is Debye temperature and ω_0 is a constant that need to be determined from the static limit of the above expression,

$$\omega_{cp}(T, \omega \rightarrow 0) = \frac{\omega_p^2}{4\pi\sigma(0)} = \omega_0 \left[4 \left(\frac{T}{\theta} \right)^5 \int_0^{\theta/T} \frac{z^4 dz}{(e^z - 1)(1 - e^{-z})} \right] \quad (6)$$

Where $\sigma(0)$ is the d.c. conductivity.

$$\omega_{ce}(T) = \frac{1}{12} \pi^3 \frac{\Gamma \Delta}{\hbar E_F} [(k_B T)^2 + (\hbar\omega/2\pi)^2]$$

Where Γ is a constant giving the average over the Fermi surface of the scattering probability, Δ is the fractional Umklapp scattering, and E_F is the free-electron Fermi energy. Basing on the equations mentioned above, the temperature dependent dielectric constant of the gold nanoparticle can be obtained. According to discrete dipole approximation (DDA), the temperature dependent extinction spectra of gold nanoparticles can be theoretically calculated.⁹⁴ The calculated spectra are shown in Figure 3-17. It shows the extinction spectra of gold particle with 50 nm diameter at different temperature from 30 to 200°C. As temperature increases, the surface plasmon resonance peak intensity decreases and the width become broadened due to the increase in damping of the gold. In addition, the surface plasmon resonance peak shifts to long wavelength direction at elevated temperatures. This can be understood from the dispersion



relation for surface plasmon waves, together with the decrease in plasmon frequency and increase in collision frequency in the Drude model as the temperature increases.

Figure 3-17 Theoretical calculated extinction spectra of a gold particle with 50 nm diameter at different temperature from 30 to 200°C.

Figure 3-18 shows the surface plasmon peak shift of a gold nanoparticle with a diameter of 50nm at different temperatures, which can be derived from the data shown in the last figure. It shows that surface plasmon resonance peaks increase linearly at range from 25°C to 200 °C. The overall comparison between the simulation results and the experimental data is qualitatively reasonable, where the surface plasmon peak of gold nanoparticles shift to long wavelength directions. However, compared to the obtained experimental data (show in Figure 4-10), the calculated wavelength shifts are larger than that from experiment. This is likely because half of gold nanoparticles are embedded in glass substrate. While in the simulation, it didn't take care of the substrate and embedding. In reality the temperature also affects the dielectric constant of the substrate, so the substrate also contributesto the surface plasmon resonance of gold nanoparticles. In addition, we only consider the single isolated nanoparticles, while it is highly possible that the particles can be coupled together in the obtained nanoparticle arrays.

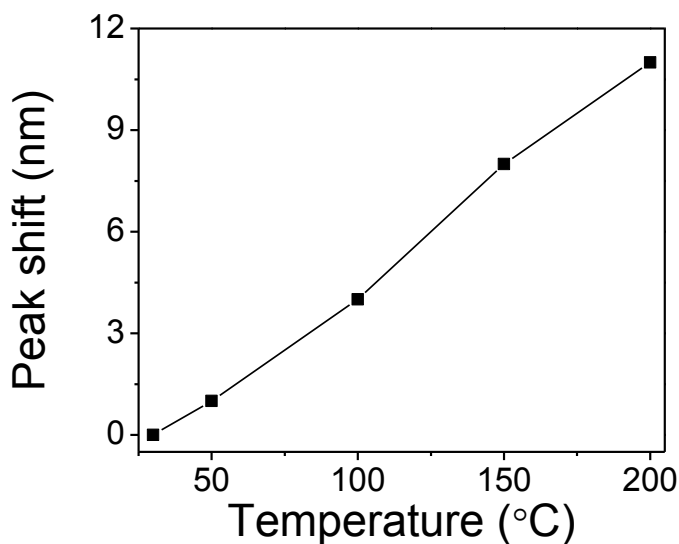


Figure 3-18 Simulated LSPR peak shift versus the temperature.

3.2.4.6 Stability of Gold Nanoparticle Arrays

Application of gold nanoparticle arrays as LSPR transducers requires stability of structural (e.g., adhesive to the supporting substrate) as well as the optical response toward dipping in solvents and drying or exposing to normal or extremely harsh environments. The stability of the morphology and optical response of gold nanoparticle arrays annealed at high temperatures (partially embedded in glass substrate) are evaluated. Figure 3-19 shows the extinction spectra of gold nanoparticle arrays that have been annealed at 600°C for 10h before and after putting in ambient conditions for 1 month. It shows that no difference is observed (LSPR peak position and intensity). Furthermore, the gold nanoparticles exposed to different solvents also obtained the similar results. All of these experiments suggest the exceeding stability

of fabricated plasmonic nanostructures. Meanwhile, a stabilizing coating is not needed is a marked advantage in terms of system sensitivity, which is very common for the nanoparticles dissolved in the solution. The new application of this highly stable plasmonic nanostructure for mass detection will be described in detail at chapter 4.

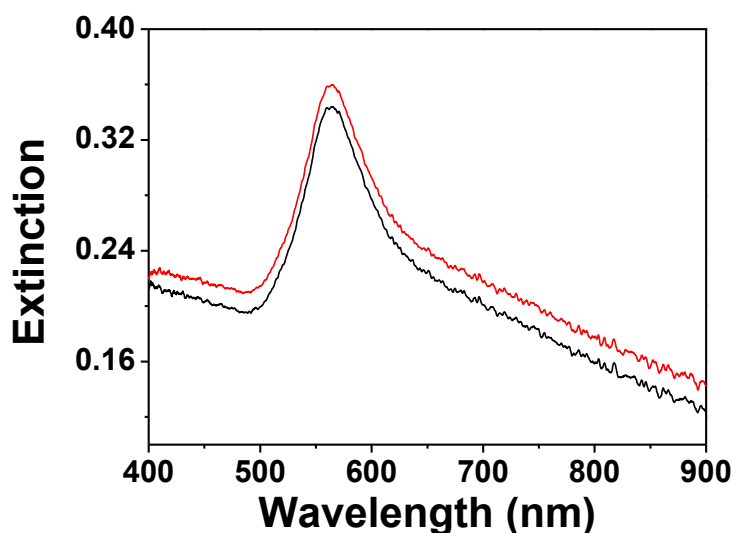


Figure 3-19 Extinction spectra of annealed gold nanoparticle arrays before (black) and after (red line) putting in ambient condition for 1 month.

3.2.4.7 X-ray Diffraction Characterization

X-ray diffraction (XRD) analysis is carried out on a Rigaku powder diffractometer using Cu-K α radiation at 40 kV and 30 mA. Figure 3-20 is the XRD spectra of gold nanoparticles deposited on glass substrate before and after thermal annealing at 300, 400, 500 and 600 °C for 10 hours (from low to high). The broad background of XRD curve collected before annealing is because of the amorphous nature of the glass substrate. After thermal annealing it shows that the diffraction peak of gold (111) plane becomes stronger as the annealing increase while keeping

the annealing time constant. This results suggests that more (111) or larger (111) facet are coming out after the samples are annealed at higher temperature and cooled down to room temperature.

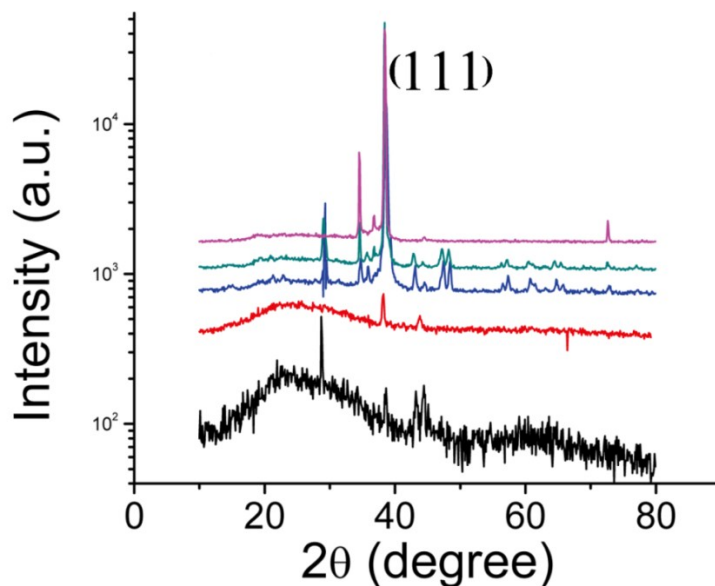


Figure 3-20 XRD spectra of gold nanoparticles deposited on glass substrate before and after thermal annealing at 300, 400, 500 and 600 °C for 10 hours (from low to high).

Surface-energy considerations are crucial in understanding and predicting the morphology of noble-metal nanocrystals. Surface energy, defined as the excess free energy per unit area for a particular crystallographic face, largely determines the faceting and crystal growth observed for particles at both the nano- and meso- scale. For a material with an isotropic surface energy, such as an amorphous solid or liquid droplet, total surface energy can be lowered simply by decreasing the amount of surface area corresponding to a given volume. The resulting particle shape is a perfectly symmetric sphere. Noble metals, which adopt a face-centered cubic (fcc) lattice, possess different surface energies for different crystal planes. This anisotropy results in

stable morphologies where free energy is minimized by particles bound by the low-index crystal planes that exhibit closest atomic packing.

The surface energy is defined as the work that needs to be done to cleave a crystal along a certain plane thereby exposing two faces or facets. To calculate the energy we need to account for the number of bonds that will be broken in the process. If an atom type, each with n_i dangling bonds of energy $2\varepsilon_i$ (that should take care of the two dangling bonds created on both the new surfaces), has density ρ_i , then the surface energy density, γ (i.e. surface energy per unit area) will be given by

$$\gamma = \sum \rho_i \cdot n_i \cdot \varepsilon_i$$

For FCC unit cell, atoms are at the corners and the face centers. Let us calculate the radius of these atoms. Place the atoms so that they touch the nearest neighbors. For the (100) face, when an edge length is a , the diameter of the atom equals $\sqrt{2}/2 a$ or $0.707a$.

Cut the FCC crystal to expose the (100) face. The (100) face contains a total of 2 atoms (1 face-centered atom + 4 quarter atoms on the corners). The central atom has four nearest neighbors below, four in the plane and therefore has four dangling bonds pointing out of the plane. Since the corner atoms contribute a fourth, we need to count only a quarter of the dangling bonds per atom, i.e. 1 per atom. That makes a total of 8 dangling bonds in an area a^2 . The surface energy density, γ_{FCC} is therefore $8\varepsilon/a^2$.

Next, I move onto the (110) plane. The plane can be easily constructed by taking one edge and its diametrically opposite edge. The area comes out to be $\sqrt{2}a^2$. This gives us 2 atoms

on the plane-four 1/4th atoms and two 1/2 atoms (at the face center positions). Each atom is bonded to two surface atoms and five atoms below it and therefore has five dangling bonds. The surface energy density comes out to be $\gamma = 5\sqrt{2}\epsilon/a^2$.

A little more courage brings us to the (111) plane. The area of the rhombus (single atom unit cell) is $\sqrt{3}a^2/4$. Each atom is bonded to 3 atoms below the plane and six in the plane, giving rise to three dangling bonds. The surface energy density is $\gamma = 4\sqrt{3}\epsilon/a^2$.

From the above calculation, for FCC crystal, the surface energy for different planes are as the following sequence: $\gamma_{(110)} > \gamma_{(100)} > \gamma_{(111)}$. And the details for FCC structured crystals are shown in the following table (Table 3-1). My experimental results can be explained in this table. When annealing for gold nanoparticles (FCC structure), (111) has lowest surface energy. So X-ray diffraction can easily detect the (111) plane.

Structure (plane)	Density of atoms	Dangling bonds/atom	Surface energy (γ)
FCC (100)	$2/a^2$	4	$8\epsilon/a^2$
FCC (110)	$\sqrt{2}/a^2$	5	$5\sqrt{2}\epsilon/a^2$
FCC (111)	$4/a^2$	3	$4\sqrt{3}\epsilon/a^2$

Table 3-1 Details of FCC structured crystals.

3.2.5 Gold Nanoparticles Arrays on Quartz

3.2.5.1 Thermal-induced Shape Transformation

Figure 3-21 shows the AFM images of gold nanoparticle arrays on the quartz substrate before and after annealing at 600 °C for 10 hours at ambient condition. The average diameter and interparticle distance are about 100 and 230 nm (Figure 3-21A), respectively. The heights of nanoparticles measured from the cross sections of AFM image are 40 nm. Although some nanoparticles combine with each other and form a long chain, which is because of not perfect close-packed polystyrene nanospheres monolayer, such structure has optical response in far infrared region and will not effect the measurement in visible wavelength region. After annealing the sample at 600 °C for 10 hours, triangle-shaped nanoparticles change to hemispherical shape (Figure 3-21B). This result is similar to that happens on shape transformation of gold nanoparticle arrays on glass substrate.

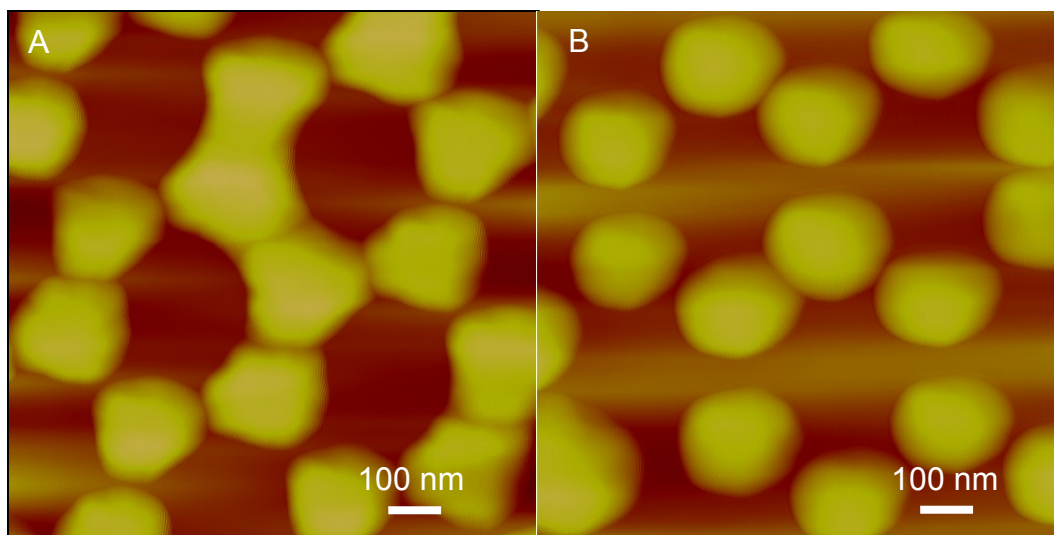


Figure 3-21 AFM images of gold nanoparticle arrays on the quartz substrate before (A) and after (B) annealing at 600 °C for 10 hours.

For quartz substrate, the soften temperature is around 1600 °C and it is much higher than our annealing temperature of 600 °C. It is also higher than the temperature of borosilicate glass (820°C), which is also used in this experiment. Although the shape of gold nanoparticles will change when annealing at high temperature, it is still sitting on the quartz substrate surface and not embedded in the substrate, which is different from that of borosilicate glass. In order to prove this, the gold nanoparticles are etched off from the substrate and AFM characterization is taken. Figure 3-22 shows an AFM image of quartz substrate after the gold nanoparticles are etched off from the surface by using aqua regia solution for 20min. It shows that there is a thin layer with the thickness of 2nm left on the surface, which is chromium adhesion layer that evaporates onto the substrate prior gold thin film evaporation and cannot be etched off.

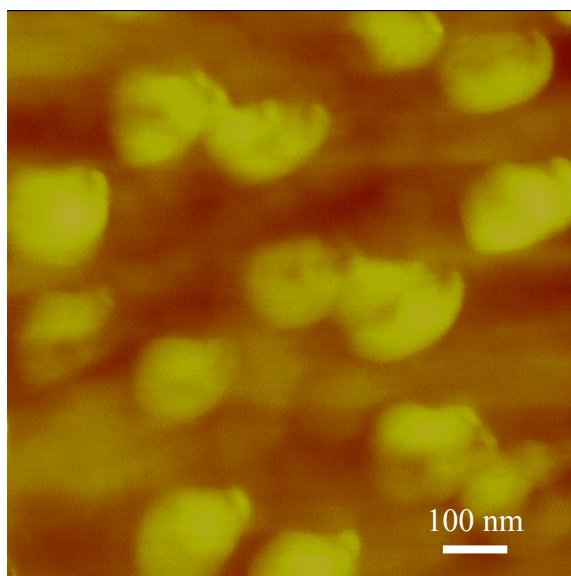


Figure 3-22 AFM images of nanohold arrays on the glass substrate after etching off high temperature annealed gold nanoparticle arrays.

3.2.5.2 Temperature Effect on LSPR

The extinction spectra of gold nanoparticles on the quartz substrate before and after annealing at 600 °C for 10 hours are shown in Figure 3-23, where the peak at 544 nm (corresponding to the quadrupole) becomes stronger and the peak at 773 nm (corresponding to the dipole excitation) disappear after annealing. Although the substrate is different, the result is similar as that obtained from the glass substrate. Meanwhile, the stability test is also taken and it is also similar with that from the gold nanoparticle arrays on glass substrate. The advantage of making the gold nanoparticles on quartz substrate is that such devices can be used at the operation temperature range and can be out of the melting temperature of gold nanoparticles, which is 1063 °C for bulk gold and the detailed can be found at the following section.

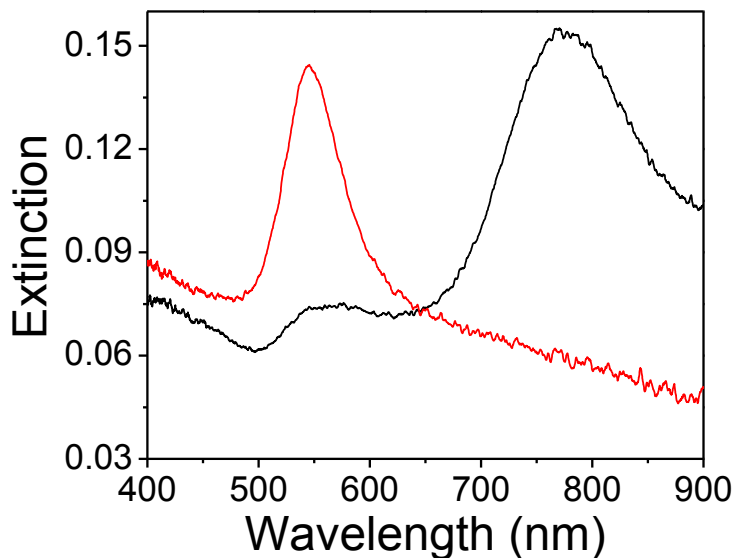


Figure 3-23 Extinction spectra of gold nanoparticle arrays on the quartz substrate before (black curve) and after (red curve) annealing.

3.2.5.3 Temperature-dependent Extinction Spectrum

Figure 3-24 shows the extinction spectra of the gold nanoparticle arrays on a quartz substrate as a function of temperature from 25°C to 1050 °C, which is expected to undergo a transition to the liquid phase within the measured temperature range. The melting temperature of solid nanoparticles depends on their size. When the sizes of nanoparticles are smaller than 20nm, the surface atoms contribute more in reducing melting temperature. But, the melting temperature is exponentially dependent on size, which makes it difficult to control melting temperatures by controlling nanoparticle sizes. This is because a small size variation will cause large deviations from the melting temperature. Larger nanoparticles with diameter over 20nm melt at the same melting temperatures as their bulk counterparts. The gold nanoparticles are larger than critical

size of 20nm, so the melting temperature should be the same as their bulk counterparts. As the temperature increase, the LSPR peak broadens and shifts to long wavelength. The broadening of the LSPR arises from the temperature dependence of the electron-phonon contribution. When the temperature reaches up to 1100°C, the LSPR peak of gold nanoparticles disappears because of melting of the gold nanoparticles. The increasing asymmetry of the band is because of the melting of the ion core.⁹⁵

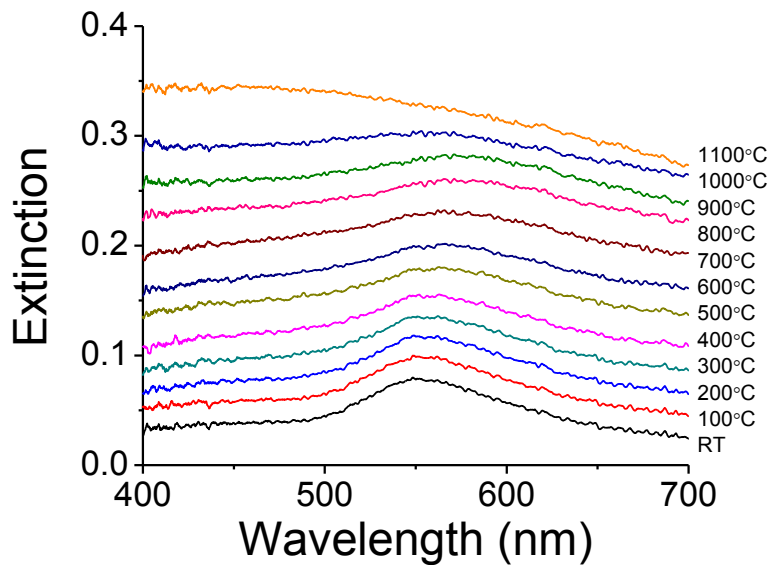


Figure 3-24 Extinction spectra of gold nanoparticle arrays on quartz substrate under different temperatures.

3.3 Conclusions

Triangular gold nanoparticles arrays, deposited on glass substrates using polystyrene nanospheres as a mask and subjected to post thermal annealing at a temperature T (600°C) in the vicinity of the substrate glass transition T_g after removing polystyrene nanospheres, transform to spherical shape and undergo partial embedding in the glass substrate. The embedded nanoparticles are exceedingly stable toward immersion in solvent, drying or exposed to ambient condition for long time. The optical response of highly stable gold nanoparticles arrays versus the temperature is reversible when increasing or decreasing the temperature, which supplies a good platform for thermal analysis. Meanwhile, the highly stable gold nanoparticle arrays are also made on quartz substrate and the optical response of gold nanoparticles up to the melting point of bulk gold are recorded. It shows that the surface plasmon resonance peak is disrupted when the gold nanoparticles melt.

CHAPTER 4: THERMAL ANALYSIS BASEDON STABLE GOLD NANOPARTICLE ARRAYS

4.1 Introduction

Instead of utilizing mechanical or electrical approaches to achieve high mass sensitivity, I have used localized surface plasmon resonance properties of an ordered array of gold nanoparticles to derive the masses of thin films of adsorbed organic molecules, which can also be removed by raising the temperature of nanoparticles (Figure 4-1). In the plasmonic nano-balance, the extinction peaks of the surface plasmon of gold nanoparticles shift linearly as the mass of loaded material increases before reaching the upper limit of mass detection. Upon desorption of materials in a programmed temperature rise process, the extinction peaks of surface plasmon resonance (LSPR) returns to the original position after all of the molecules are desorbed. Within the maximal detectable limit, the peak shift is proportional to the mass loaded on the gold nanoparticles. The superior mass sensitivity of plasmonic nano-balance, combined with the in-situ and remote detection capability and high temperature operation of plasmonic nanosensors, allows the ultrasensitive mass detections and temperature programmed analysis of loaded organic materials.

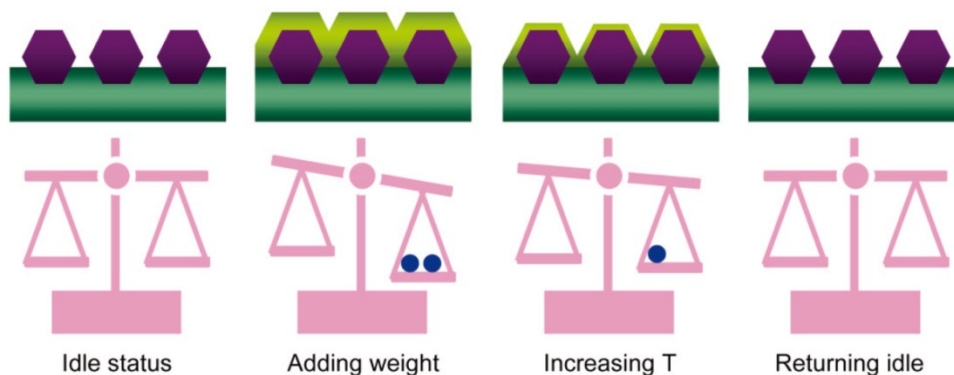


Figure 4-1 Schematic illustration of ultra-sensitive plasmonic nano-balance.

4.2 Results and Discussion

4.2.1 Detection of Wax Adsorption

In order to derive the mass-dependence of the plasmonic nano-balance, thin films of paraffin (melting temperature of 56 °C) are thermally deposited layer-by-layer onto an annealed gold nanoparticle arrays by using simple thermal evaporation method. The thicknesses are controlled by exposing gold nanoparticle arrays to paraffin vapor for different period of time (1 to 10 min), and are verified by using the height measurement of AFM. A few papers have pointed out the response of LSPR to adsorbed layers can be carried out by calculation and experiments. When the thickness of adsorbed layers is much thinner than the characteristic decay length of electromagnetic field, the shift of LSPR extinction peak is proportional to the thickness of adsorbed layers, namely linear-response regime. For the thicker layers, the peak response to the thickness is beyond the linear regime and the LSPR peak will not shift although the thickness

of adsorbed layers increased. In the current experiments, all the analysis data are based on the linear-response regime. As shown in Figure 4-2, with the increase of paraffin layer thickness, the LSPR peak shifts toward long wavelength direction and will cease to increase when the thickness of wax is reached at the upper limit level.

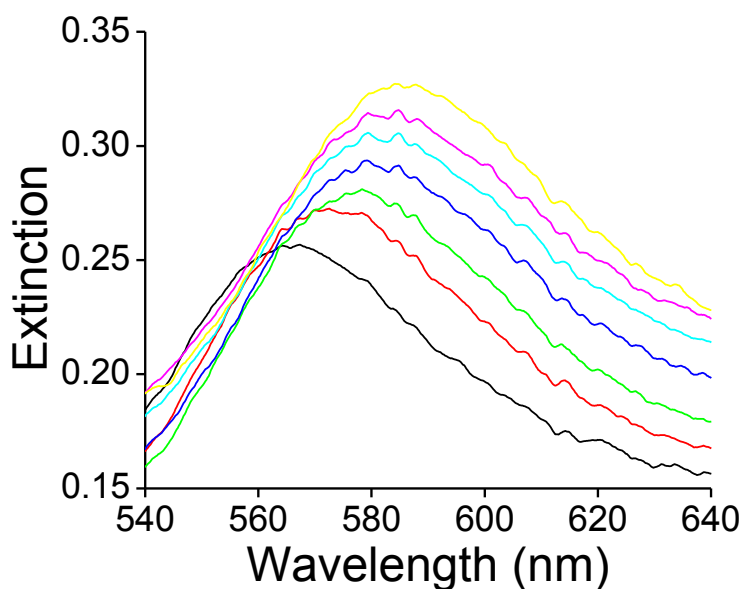


Figure 4-2 Extinction spectra of gold nanoparticle arrays after exposing to wax vapor for different times.

After depositing a certain number of layers on the gold nanoparticle arrays, the $\Delta\lambda_{\max}$ stops responding to the layer thickness. Considering the density (0.9 g/cm³) and molecular weight (228) of the paraffin and the maximum thickness of the layer (40 nm), the maximal measurable mass is about 36 ng, and the detection sensitivity in air can be derived as 0.77nm/ng in the linear region (Figure 4-3) basing on the light spot area of 2 mm². Although the packing density of molecules depends on how fast the film is deposited or whether the film is thermally

annealed, the films in this experiment are deposited at relatively slow rate (~ 4 nm / min), thus the density of the paraffin film could be considered close to that of bulk material.

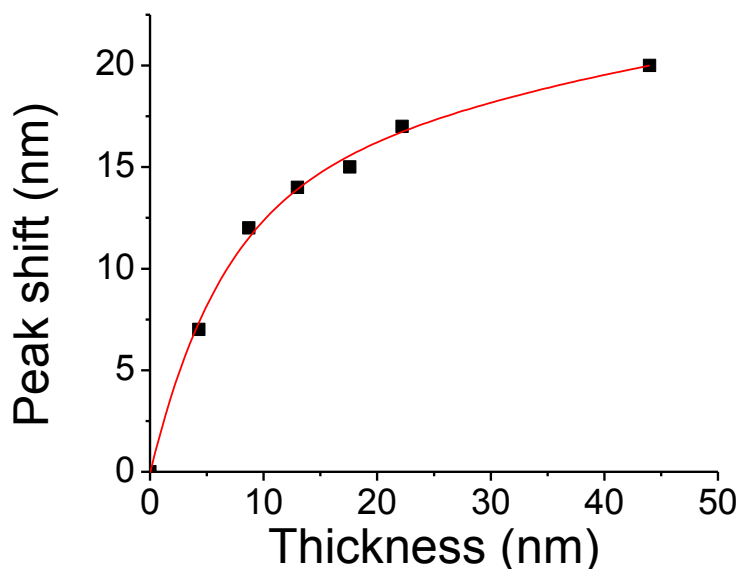


Figure 4-3 LSPR peak shift versus the thickness of wax films.

4.3.2 Thermal Analysis of Wax Desorption

The temperature-programmed thermal analysis is carried out by heating gold nanoparticles arrays that are covered by paraffin thin films, and monitored LSPR signals continuously. Figure 4-4 shows that the LSPR peak shifts toward short wavelength direction as temperature increases due to desorption of paraffin molecules. The temperature that LSPR peak shifts most corresponds to desorption of paraffin. Mass loss kinetics shows the similar trend as that of thermogravimetric analysis: the curves shift to higher temperatures at higher heating rates.

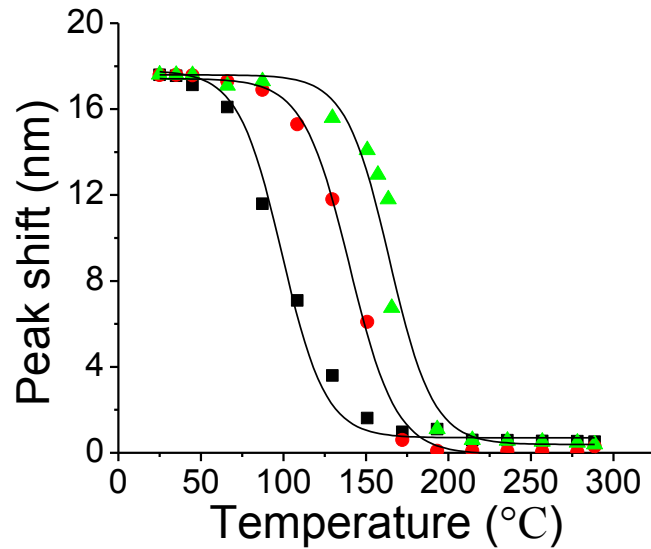


Figure 4-4 SPR peak shift of wax coated nanoparticles versus the temperature at different heating rates, where square, circle, and triangle are collected at 2, 5, and 10 °C/min.

The temperature-programmed thermal analysis is carried out by heating gold nanoparticles with paraffin thin films and monitoring SPR signals continuously. Figure 4-4 shows that the LSPR peak shifts toward short wavelength direction as temperature increases due to desorption of paraffin molecules. The temperature that LSPR peak shifts most corresponds to desorption of paraffin. Mass loss kinetics shows the similar trend as that of thermogravimetric analysis: the curves shift to higher temperature at a higher heating rate.

The Arrhenius equation,

$$k = A \exp\left(-\frac{E}{RT}\right) \quad (1)$$

is almost universally assumed for the temperature dependence of k , where A (the pre-exponential factor) is usually assumed to be independent of temperature, E is the energy of activation, and R is the gas constant.

It is assumed that the isothermal rate of conversion (da/dt) is a linear function of a single temperature-dependent rate constant (k) and some temperature-independent function of the conversion (C), i.e.,

$$\frac{d\alpha}{dt} = kf(\alpha) \quad (2)$$

Substituting eq (1) into eq (2), the thermal mass-loss kinetics can be expressed in the following form:

$$\frac{d\alpha}{dt} = Af(\alpha)\exp\left(-\frac{E}{RT}\right) \quad (3)$$

where α is the degree of conversion, t is the time, A is the pre-exponential factor, E is the activation energy, R is the gas constant and $f(\alpha)$ is the differential conversion function.

If we induce the heating rate into the eq (3), then one obtains

$$\frac{d\alpha}{dt} = \beta \frac{d\alpha}{dT} = Af(\alpha)\exp\left(-\frac{E}{RT}\right) \quad (4)$$

Rearranging eq (4) and integrating both sides of the equation leads to the following expression

$$g(\alpha) = \frac{A}{\beta} \int_{t_0}^t \exp\left(\frac{-E}{RT}\right) dT = \left(\frac{AE}{\beta R}\right) p(u) \quad (5)$$

Where $p(u) = \int_{\infty}^u -\left(\frac{e^{-u}}{u^2}\right)du$ and $u = \frac{E}{RT}$

For the non-isothermal conditions with a linear heating program (heating rate is β), Flynn-Wall-Ozawa isoconversional integral method (FWO) uses the Doyle approximation to approximate the above relation. This method is derived from the integral method. The technique assumes that A , $f(\alpha)$ and E are independent of T while A and E are independent of α . Then eq (5) may be integrated to give the following result in logarithmic form, which gives:^{96, 97}

$$\ln g(\alpha) = \ln\left(\frac{AE}{R}\right) - \ln \beta + \ln p\left(\frac{E}{RT}\right) \quad (6)$$

Using Doyle's approximation for the integral, which allows for $E/RT > 20$, eq (6) can be simplified as the following:

$$\ln \beta = \ln \frac{AE}{Rg(\alpha)} - 5.331 - 1.052 \frac{E}{RT} \quad (7)$$

Thus, at the same mass loss, a plot of $\ln \beta$ versus $-1/T$ should be a straight line. The activation energy can be derived from the slope of the regression line. The $\ln \beta$ versus $-1/T$ is plotted from 20 to 80% conversion for the mass loss of paraffin over gold nanoparticle arrays (Figure 4-5), where the effect of temperature on gold nanoparticles has been considered and subtracted. The lines at different mass loss values are approximately parallel to each other and all correlation coefficients of linearity are over 0.98. Moreover, the average activation energy calculated from these plots is 32 kJ/mol.

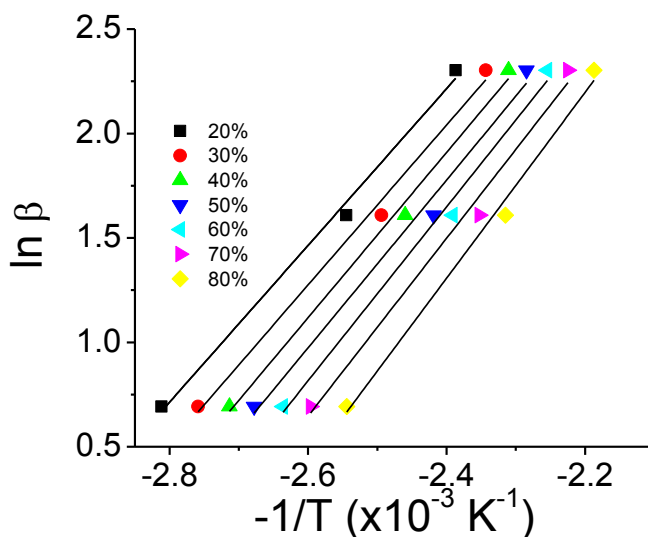


Figure 4-5 Plot of $\ln\beta$ versus $-1/T$.

4.3.3 Detection of octadecylamine Absorption and Thermal desorption

The sensitivity of mass detection is dependent on the nature of materials deposited on the array of nanoparticles. We have studied the shifts of LSPR peaks of an array of annealed gold nanoparticles as functions of the thickness of octadecylamine. Figure 4-6A shows the extinction spectra of gold nanoparticles after exposed to the octadecylamine vapor from 10 to 120 seconds. In contrast to paraffin that has weak interaction with gold, octadecylamine has relatively stronger interaction with gold. As the film becomes thick, the LSPR peak shifts linearly to longer wavelength direction until the thickness is 20 nm, where the peak does not shift (Figure 4-6B). The mass detection range (28 ng) is lower than that of paraffin film, meaning the detection sensitivity is higher.

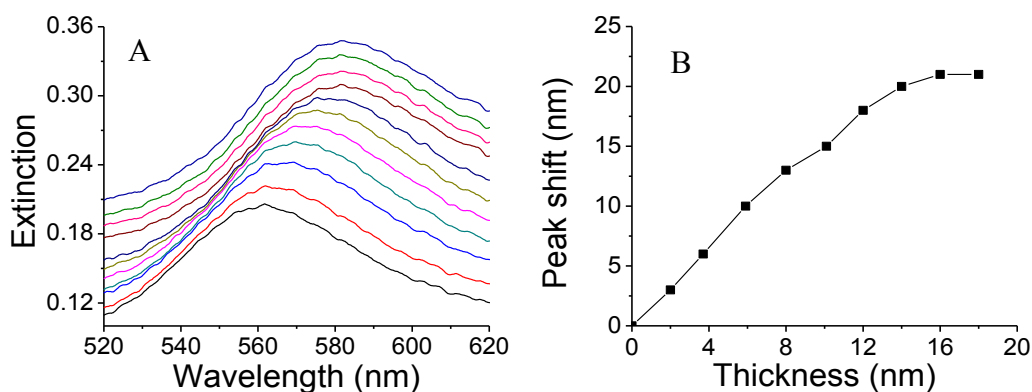


Figure 4-6 Extinction spectra of gold nanoparticle arrays after exposed to octadecylamine vapor for different times (A), SPR peak shift versus the thickness of octadecylamine thin films (B).

The LSPR peak shifts to short wavelength and returns to original position as the temperature increases linearly (Figure 4-7), suggesting octadecylamine molecules are desorbed. The desorption is reflected in the intensity change of LSPR peak, where octadecylamine desorption leads to an increase of transmission magnitude. In the case of thiol molecules that form strong bonds with gold atoms, the sensitivity of mass detection is lower.

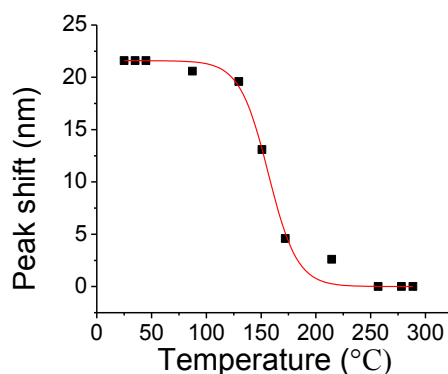


Figure 4-7 LSPR peak shifts upon the desorption of octadecylamine from gold nanoparticles at heating rate of 5 °C /min.

Figure 4-8A shows that the LSPR peaks of octadecylamine-coated gold nanoparticles (annealed) shift to short wavelength direction as the temperature increases linearly (from low to high). The LSPR peak shifts to short wavelength and returns to original position as the temperature increases linearly, suggesting octadecylamine molecules are desorbed completely. Desorption is also reflected in the absorbance change at the initial peak position (Figure 4-8B), where desorption of octadecylamine leads to an increase of transmission value.

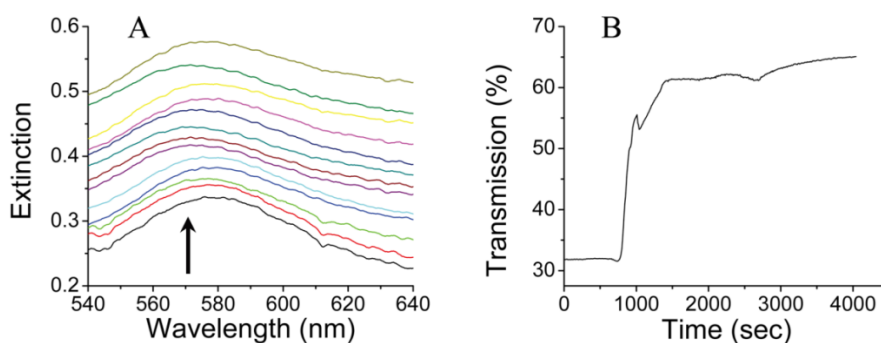


Figure 4-8 (A) Extinction spectra of gold nanoparticles coated by octadecylamine thin films as temperature increases linearly (from low to high); (B) The transmission change of peak intensity of gold nanoparticles covered by octadecylamine versus time as temperature increases.

4.3.4 Detection of DNT Absorption and Thermal Desorption

TNT(2, 4, 6-trinitrotoluene) is an important explosive since it can quickly change from a solid into hot expanding gases. The analysis of trace TNT or their derivatives attracts a lot of attention due to its high demand for homeland security needs in a wide variety of scenarios such as mail sorting centers, airports and luggage, transit centers, and other civilian situations. Driven by those needs, I demonstrate the trace detection of one type of TNT's derivative, 2, 4-dinitrotoluene (DNT), by using fabricated gold nanoparticles arrays.

The plasmonic nano-balance was used to measure the mass of a thin film of 2, 4-dinitrotoluene (DNT), which is a derivative of highly explosive 2, 4, 6-trinitrotoluene (TNT). The thin film of DNT (melting temperature of 71 °C) is thermally deposited on annealed gold nanoparticles. Figure 4-9A shows the extinction spectra of gold nanoparticles before and after exposing to 2,4-dinitrotoluene (DNT) vapor for a period of time ranging from 5, 10, 15, 20 and 25 seconds (from low to high). As the deposit time increases, the LSPR peak shifts to long wavelength direction and then cease to shift as the deposition time exceeds 15 seconds. Not only can the absorption of DNT be detected, desorption of DNT can also be detected by measuring the extinction spectrum. Figure 4-9B shows the transmission spectrum by recording the transmission change of the LSPR peak intensity. As the temperature increases, the transmission value will increase gradually and then reach a stabilized level, which means all of DNT molecules have been removed by the temperature-programmed rise process.

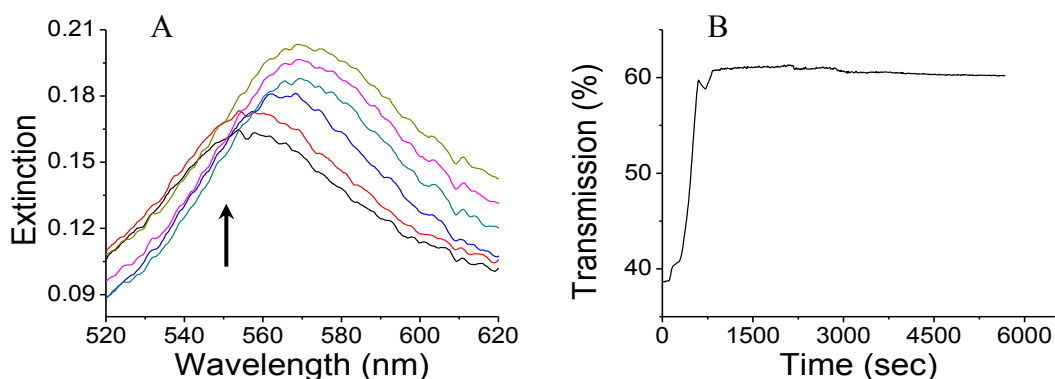


Figure 4-9 (A) Extinction spectra of gold nanoparticles after exposing to 2,4-dinitrotoluene for a period of time ranging from 5, 10, 15, 20 and 25 seconds (from low to high); (B) The transmission change of peak intensity of gold nanoparticles covered by 2, 4-dinitrotoluene versus time as temperature increases.

Figure 4-10 shows the peak shifts as a function of temperature, where the maximal desorption occurs at 160 °C. Desorption is also reflected in the increase of transmission magnitude. According to the theoretical calculation by the method that mentioned above, the sensitivity of mass detection is 0.77 nm/ng, which is close to those of paraffin wax and octadecylamine.

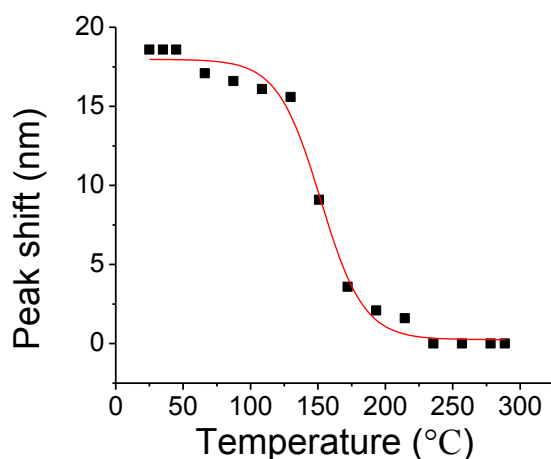


Figure 4-10 SPR peak shifts upon desorption of 2, 4-dinitrotoluene from gold nanoparticles at heating rate of 5 °C /min.

4.3.5 Detection of Thiol Molecular and Thermal Desorption

Not only the materials thin film can be detected, but also the thiol molecular self-assembled monolayer can be detected. The surfaces of gold nanoparticles are modified by incubating in 5mmol l, 10-decanedithiol ethanolic solution for 24 hours to form a monolayer of thiol molecules because of the formation of strong gold-sulfur covalent bond. Figure 4-11 shows the extinction spectra of high-temperature annealed gold nanoparticles before and after surface

modification. For surface modified gold nanoparticles, the LSPR peak shifts to long wavelength direction from 560nm to 584 nm compared with bare gold nanoparticles.

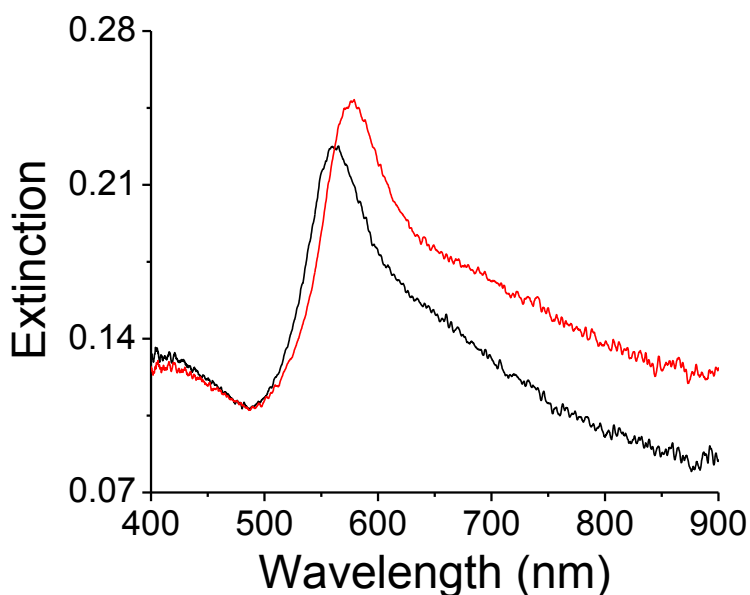


Figure 4-11 Extinction spectra of gold nanoparticle arrays in air before (black line) and after (red line) modified by 1, 10-decanedithiol.

For gold nanoparticles that have been modified by 1, 10-decanedithiol, the sample is then heated up gradually to high temperatures to remove the thiol molecules by using a temperature-programmed rise process. Figure 4-12 shows extinction spectra of the sample that was recorded at different temperatures. As the temperature increases, the LSPR peak shifts to short wavelength direction, and then cease to shift around 300 °C. The LSPR peak shifts demonstrates desorption of thiol molecules from gold nanoparticles surfaces and cease of peak movement suggest all of the thiol molecules have been removed from the gold nanoparticle surfaces.

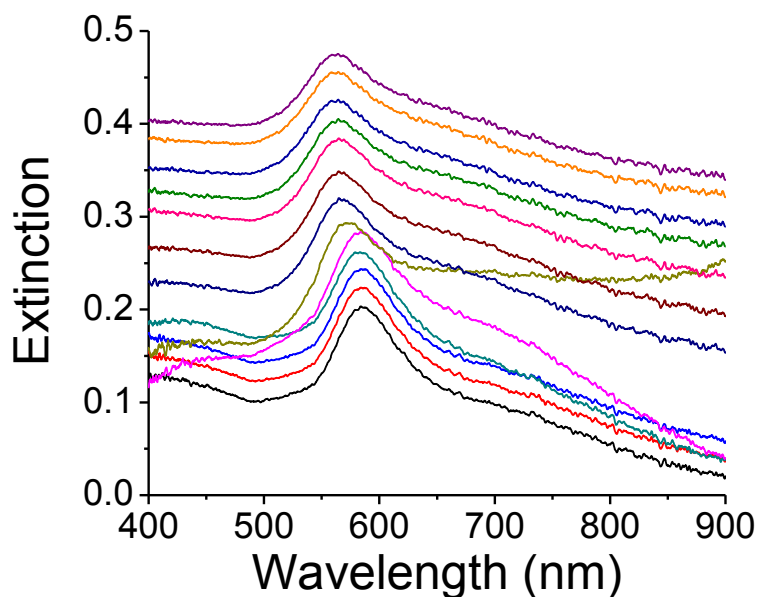


Figure 4-12 Extinction spectra of 1, 10-decanedithiol molecules modified gold nanoparticles at different temperatures from 25°C to 300 °C (bottom to up).

Figure 4-13A shows the shift of LSPR peaks as a function of temperature. As the temperature increases, the LSPR peak shift becomes smaller and smaller compared to the original peak shift. It is noted that the temperature effect for the LSPR peak shift has been considered and taken off. As the temperature increases, the LSPR peak of bare gold nanoparticles shifts to long wavelength, so the negative peak shift (shown in Figure 4-13A) is only coming from desorption of thiol molecules. Figure 4-13B is a corresponding derivative curve of 4-12A, where the maximal rate of desorption occurs at 150 °C.

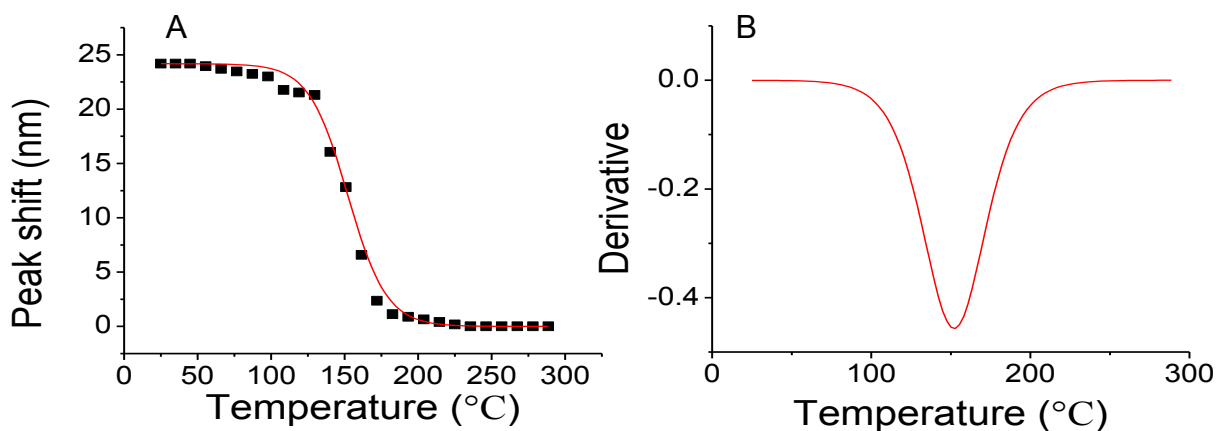


Figure 4-13 SPR peak shifts upon the desorption of 1,10-decanedithiol (A) and its corresponding derivative curve (B) from gold nanoparticles at a heating rate of 5 °C /min.

Assuming that nanoparticles are hemispheres, the surface area of single gold nanoparticles (radius of 25 nm) available for self-assembled monolayer (SAM) is calculated to be $3.9 \times 10^{-11} \text{ cm}^2$. Given that the packing density of 1,10-decanedithiol molecules on gold surface is 4.4×10^{14} per square centimeter,⁹⁸ the sensitivity of mass detection is about 125 nm/ng. The detection range depends on the decay length of the electromagnetic field around the nanoparticles. Due to the near-field nature of surface plasmon, the maximal thickness of film that can be detected by plasmonic nano-balance is approximately 20 nm. The maximal detectable mass of thin film can thus be derived from the density of molecules in thin film. The high mass sensitivity and thermal analysis ability of the plasmonic nano-balance provides an opportunity to measure the mass of explosive materials.

4.3.6 Theoretical Calculation of Detection Sensitivity

In the experiment, the surface area is about 2 mm², which corresponds to a minimal detection limit of 2 ng paraffin. Ideally, the active surface area can be reduced down to hundreds of micrometers by making nanoparticle arrays on the end of a multimode optical fiber.⁹⁹ Such size reduction will not affect the SPR signal, but will lower the detection limit down to sub-nano-gram level. If a 100 μm diameter optical fiber is used, the mass of paraffin can be as small as 1.8 pico gram. In the case of thiol, the detection limit could be much smaller. The extremely high mass sensitivity, combined with the remote detection ability and high temperature operation of optical sensor, would be a great benefit for temperature-programmed thermal analysis and daily mass measurements.

According to our experimental design, we define the detection sensitivity as the following equation:

$$\Delta S = \frac{\Delta\lambda_{\max}}{A \cdot h \cdot \rho}$$

Where ΔS is the detection sensitivity, $\Delta\lambda_{\max}$ is maximum SPR peak shift, A is the light sport size, h is the thickness of detected molecular thin film, and ρ is the density of the molecular. The detection sensitivity is directly proportional to the SPR peak shift and inversely proportional to the density and thickness of deposited molecules.

Based on our defined detection sensitivity equation and experimental results, the detection sensitivities are summarized in the following table (Table 4-1):

Molecular	Maximum Mass	Detection Sensitivity
Wax	36 ng	0.77 nm/ng
2,4-Dinitrotoluene (DNT)	28 ng	1.4 nm/ng
Mercury	17 ng	0.29 nm/ng

Table 4-1 Calculated detection sensitivity based on experimental results.

Our established detection system has some advantages that have been mentioned above. However, due to the surface sensitive nature of this method, the maximal detectable mass is limited and cannot be used on bulk materials. The maximal operating temperature that can be achieved by this technique is determined by the melting temperatures of gold or silver nanoparticles, which is usually lower than their bulk counterparts.¹⁰⁰ In addition, although it can work in the thermogravimetric mode, this technique cannot operate in other thermal analysis modes such as differential thermal analysis or differential scanning calorimetry. This is because the absolute heat flux cannot be measured.

4.3 Conclusions

In summary, structure stable gold nanoparticle arrays have been obtained by combining simple and low-cost nanosphere lithography and thermal annealing methods. Based on gold nanoparticle arrays plasmonic nano-balance, sub-nano-gram sensitivity has been achieved for the mass measurements in air, liquid, and temperature programmed thermal analysis. The plasmonic resonance peaks of nanoparticle arrays shift upon increasing the mass of materials, and return to original position after a linear temperature rise process. Such high mass detection sensitivity, combined with the remote detection capability and high temperature operation of the plasmonic sensors, allows the *in-situ* detections of the mass of materials, thermally desorbed molecules, and stand-off mass detection of explosive materials.

CHAPTER 5: DIRECT VISUALIZATION OF MOLECULAR ADSORPTIONS ON GOLD NANOPARTICLE ARRAYS

5.1. Introduction

I will report the detection of low concentration molecules including polymer, mercury vapor, and an explosive derivative 2,4-dinitrotoluene (DNT), by directly visualizing color changes of an ordered array of plasmonic nanoparticles deposited on glass substrates (Figure 5-1). The adsorption of molecules onto metal nanoparticles changes local dielectric constants, and optical appearance of glass substrates. In the case of mercury vapor, chronic exposure to mercury is monitored by detecting accumulated color changes of gold nanoparticles that have high affinity to form alloy with mercury. The amalgamated nanoparticles can be regenerated by heating the substrate up to a high temperature (300°C), providing a passive, low cost, and convenient way to detect mercury vapor. Gold nanoparticles can be deposited onto a large substrate to allow solid state capture of mercury, which enables simultaneous mercury sensing and capturing. In the case of explosive detection, the explosive vapor condenses on solid surface, changes local dielectric constants and leads to color changes of the substrate. In addition, polymer multilayers that have precisely controlled thicknesses have been used as a standard to reflect or calibrate the detection capability of this method.

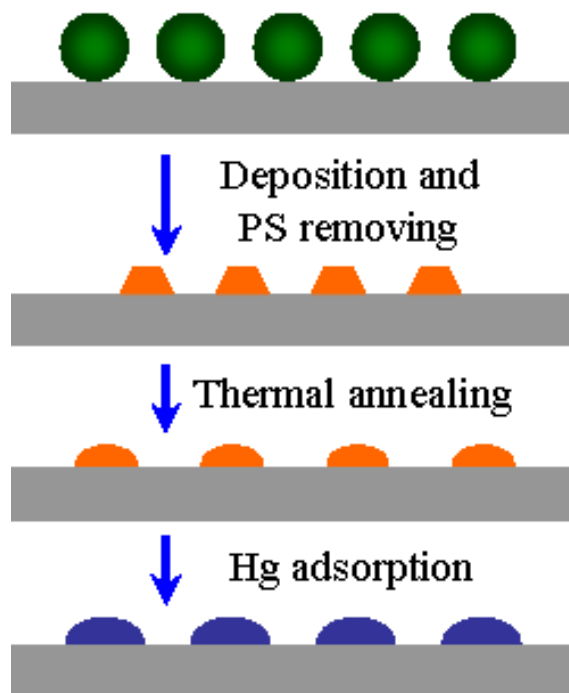


Figure 5-1 Schematic illustrations of color change of gold nanoparticles upon deposition of different molecular thin films (mercury, DNT and polyelectrolyte multilayers).

5.2 Results and Discussion

5.2.1 Visualization of Polyelectrolyte Multilayers Adsorption

Polyelectrolyte multilayers are deposited on the nanoparticle arrays through layer-by-layer (LBL) method and details of the process is described in chapter 2. UV-Vis extinction spectra of gold nanoparticles are collected in ambient conditions after depositing polyelectrolyte multilayers. Figure 5-2A shows the extinction spectra of an ordered gold nanoparticle array in dried nitrogen after depositing one to three PAH/PAA bilayers. The resonance peak shifts to long wavelength direction as the number of multilayers increases. More

interestingly, the color change of gold nanoparticles can be observed by making micropatterns on the substrate (Figure 5-2B), which allows to conveniently monitor polymer multilayers.

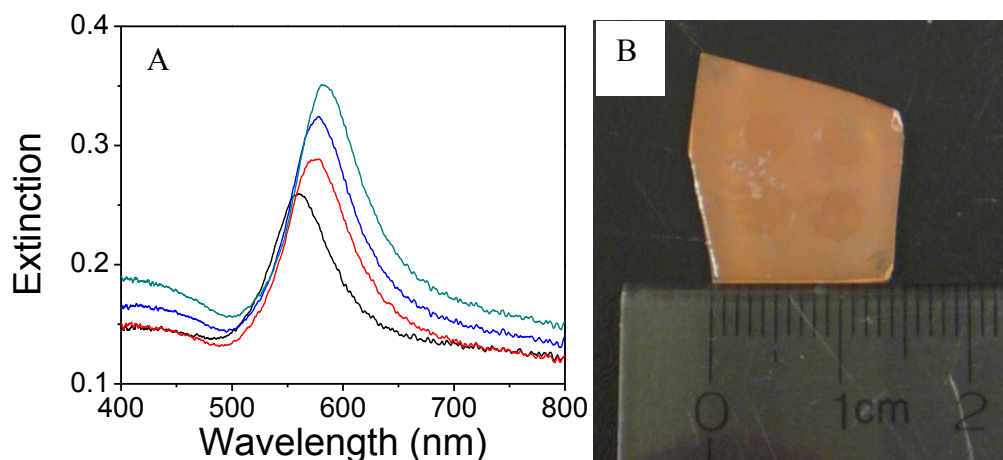


Figure 5-2 (A) The UV-Visible extinction spectra of gold nanoparticle array with 0 to 3 bilayers of PAH/PAA (bottom to top), respectively; (B) a micrograph of circular patterns that have been covered by three bilayers of PAH/PAA.

5.2.2 Visualization of 2, 4-Dinitrotoluene Absorption

TNT is one of the most commonly used explosives for military and industrial applications. The analysis of TNT and their derivatives attracts a lot of attention due to their high demand for homeland security needs.¹⁰¹ Different techniques for analyzing explosives, and particularly nitroaromatic derivatives were reported in the past decade. The current methods for detection of TNT or their derivative residue on solid surfaces commonly involve complex instrumentation such as ion mobility spectrometry, gas/liquid chromatography, mass

spectrometry, and surface acoustic wave method. These methods require frequent instrument calibration, sophisticated vapor sampling, and preconcentration procedures.¹⁰²⁻¹⁰⁵ These costly instrument-based techniques are not applicable for most of the on-site identification of TNT. Thus, a detection strategy has trended toward portable, visual, and operating ease of sensitive techniques. Due to its low vapor pressure and strong adhesion to solid surface, however, the rapid on-site identification of TNT particulates on the surface of suspicious objects is still a challenging task. The plasmonic nanostructures detection platform reported herein is promising to meet the challenge, which visualizes the color changes directly by naked eyes as the DNT attaches onto the plasmonic nanoparticles surface.

In this experiment, thin films of 2, 4-dinitrotoluene (DNT) (melting temperature of 71°C), which is a derivative of an explosive 2, 4, 6-trinitrotoluene (TNT), are thermally deposited onto annealed gold nanoparticle arrays. The thickness is controlled by exposing nanoparticles to vapor for different lengths of time (from 5 to 25 seconds), and measured using AFM. The deposited films change the local dielectric constant around the nanoparticle, and lead to shifts of localized surface plasmon resonance peaks, which is shown in Figure 5-3A. As the thickness increases, the LSPR peak shifts to long wavelength direction and ceases to increase after a 15 second deposition. Not only it can be detected by LSPR of gold nanoparticle arrays, but also can be visualized directly by naked eyes. In order to visualize it clearly, photolithography method is used to make a pattern on the glass substrate with gold nanoparticle arrays. First, a droplet of the photoresist AZ4620 is dropped in the center of the substrate, then starts spinning at 500rpm for 6sec, followed spinning at 3000rpm for 40sec. After that, the substrate is allowed to settle for 2 min on the spin stage and then carefully move the substrate to a flat and room temperature

surface. Second, the photoresist coated substrate is put on a hot plate to bake at 95°C for 5min. Third, the soft baked substrates are exposed to UV light for 10min after aligning the photomask. Finally, the substrates are developed in a developer solution of AZ400K with the ratio of 1:3 AZ400K to water for 1min. The developed substrates are rinsed with distilled water, blow dried with nitrogen and ready to use. The patterned substrate is deposited DNT thin films by exposing to its vapor for certain time. After removing the left photoresist by acetone, a clear contrast between the exposed and unexposed area (circular area) can be seen from Figure 5-3B, suggesting that the DNT thin attachment can also change the color of the gold nanoparticle arrays.

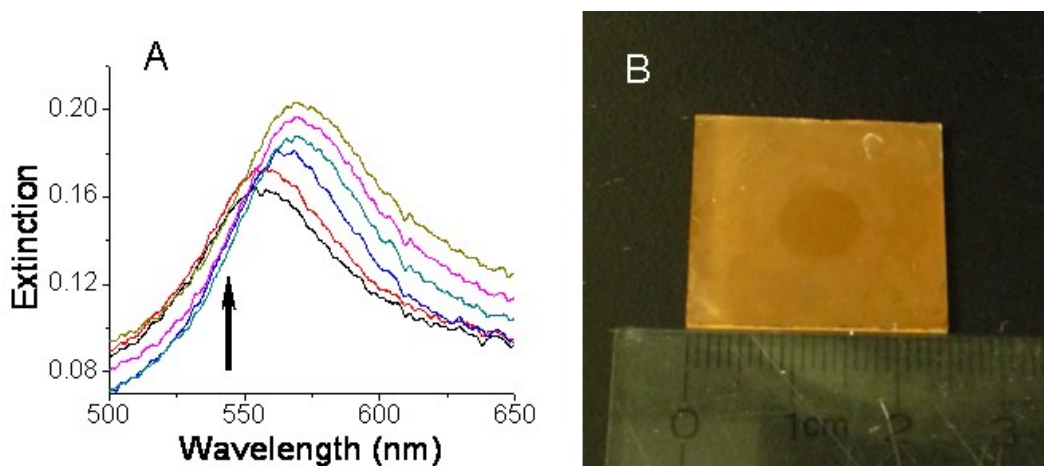


Figure 5-3 (A) The extinction spectra of gold nanoparticles after exposing to DNT vapor, where the curves are taken at 0, 5, 10, 15, 20 and 25 seconds (bottom to top), respectively; (B) a micrograph of a circle pattern not exposed to DNT.

5.2.3 Mercury Vapor Detection

Mercury is extremely toxic and must be handled very carefully. The most common source of chronic mercury poisoning is the inhalation of mercury vapor when mercury evaporates at room temperature. It is found that mercury is a potential neurotoxin, which will not degrade and is not destroyed by combustion. It can also accumulate to dangerous levels in the environment. Because mercury vapor is colorless, odorless, and tasteless (except in very high concentrations when it may cause a metallic taste in the mouth), sensing minute amounts of mercury vapor is very important to measuring air pollution in public and industrial settings in order to keep people healthy.

A variety of techniques such as optical sensors, microcantilever, conductometric sensors and quartz crystal microbalances have been used to detect mercury depending on formation of mercury alloys with gold or aluminum thin films based sensing materials.¹⁰⁶⁻¹⁰⁹ Most of these methods are expensive, require trained personnel to operate, and cannot be widely deployed over a large area. Recently a variety of nanoparticles have been used to detect gaseous species, where the changes in physical properties of nanoparticles reflect existence or concentration of target molecules. Due to the ultra-small sizes and large surface areas of nanoparticles, the detection sensitivity has been enhanced and the response time has been shortened. Gold nanoparticles have shown surface plasmonic effect. Once gold nanoparticles are assembled on a dielectric substrate, an incoming white light can excite the nanoparticles' surface plasmon, which resonates with those of nearby nanoparticles and eventually causes extinction or scattering of light. The surface plasmon resonance (SPR) peak will shift upon molecular adsorptions due to changes in the

dielectric constant of the medium, and provides a means of signal transduction. I have realized in my experiment to detect ppm level mercury vapor in air by directly visualizing the color changes of an ordered array of gold nanoparticles deposited on glass surfaces.

A glass substrate with gold nanoparticles arrays is installed inside a self-built chamber that has an inlet and outlet to allow mercury vapor to be delivered by nitrogen flow at room temperature. The concentration of mercury vapor is determined by vapor pressure of mercury at room temperature and the flow rate of nitrogen. Figure 5-4A shows the peak shifts when gold nanoparticles are exposed to 15 ppm of mercury vapor for specific length of time, where each curve is vertically shifted for display purposes. The peak shifts toward short wavelength direction from 565 to 560 nm and saturates after about 2 hours exposure. The magnitude of peak shift is plotted as the function of exposure time (Figure 5-4B), where a monotonic peak shifts can be seen. The response rate on gold nanoparticles to mercury vapor has been compared to that on gold thin film. At an exposure time of 30 min, the magnitude of the peak shift (4.25 nm) is 85% of the total peak shift (5 nm), which is faster than 67% collected on thin film.¹¹⁰ The fast response is attributed to large surface to volume ratio of nanoparticles. The nanoparticles can also be regenerated by heating the mercury exposed sample to remove mercury. When the temperature is kept at 300°C for 30 min, the plasmon resonance peak shifts to long wavelength and returns to original value. The regeneration can be done for a few times without deteriorating the sensing behaviors, which provides a passive, low cost and convenient way to detect mercury vapor.

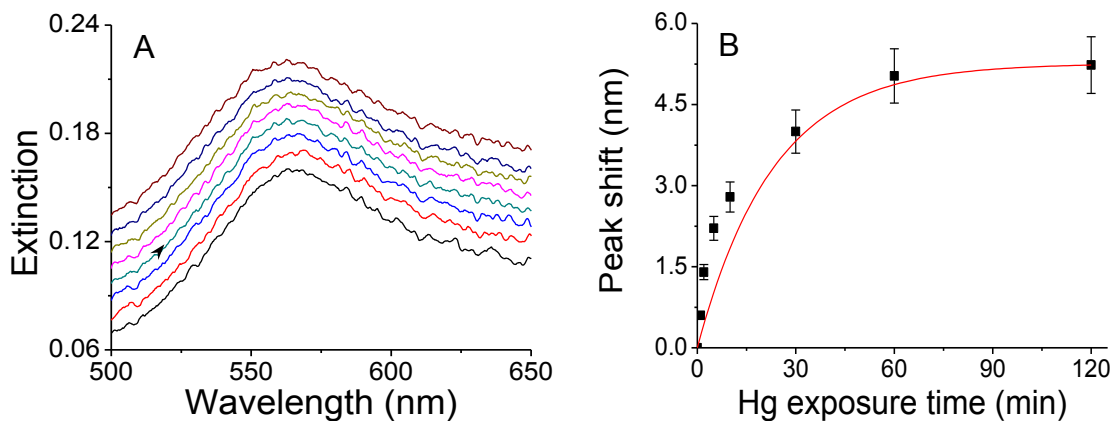


Figure 5-4 The peak shifts of gold nanoparticles after exposed to 15 ppm mercury vapor (A), where the curves are taken at 0, 1, 2, 5, 10, 30, 60 and 120 min (bottom to up), respectively; (B) the magnitude of peak shifts at different exposure time.

5.2.4 AFM Measurement

In order to confirm the origin of peak shifts, the gold nanoparticles before and after exposed to mercury vapor are imaged by AFM. Figure 5-5A and 5-5B show AFM images of gold nanoparticles before and after exposing to 15 ppm of mercury vapor for 2 hrs, respectively. Nanoparticles after exposure (Figure 5-5B) are larger than those in Figure 5-5A at the same magnification. From the cross-section profiles of images (insets of Figure 5-5A and 5B insets), the height of nanoparticles after mercury exposure is derived to be 30 nm, which is taller than before exposure (20 nm). Although the lateral dimension derived from AFM does not reflect actual value because of the broadening effect of AFM imaging, the heights of nanoparticles can be reflected accurately. If the ratio of expansion is identical in each direction, the volume increase of a hemispheric nanoparticle with height of 30 nm is 3.4 times as that of a 20 nm hemispheric nanoparticle. Taking densities of gold (19.3 g/ml) and mercury (13.5 g/ml), the gold

to mercury mass ratio is derived to be 0.6. The adsorption of mercury increases the volume of gold nanoparticles, and changes the effective refractive index, which leads to a blue shift of LSPR peaks. Although the peak shifts is relatively small (5 nm), the color change of gold nanoparticles upon mercury exposure can be visualized by the naked eye or by using an optical microscope.

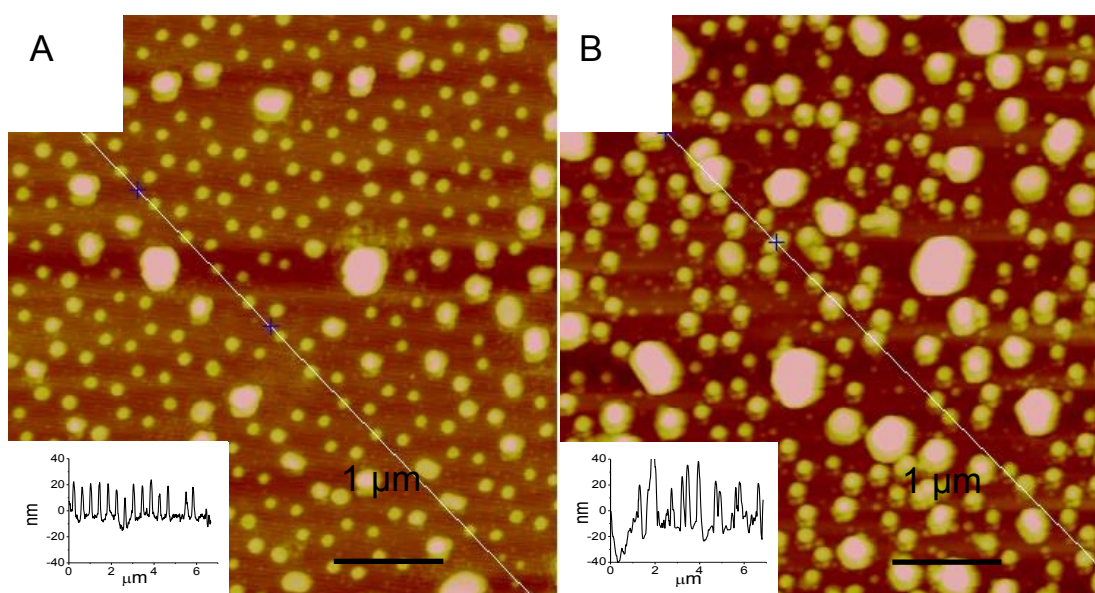


Figure 5-5 AFM images of nanoparticles before (A) and after (B) exposing to mercury for 120 min, where insets show the according cross section profiles.

5.2.5 Optical Microscopic Characterization

Micropatterns have been made on a glass substrate with an ordered array of gold nanoparticles. After forming a thin film of photoresist, the glass substrate is radiated with UV light (254 nm) through a mask. After developing the UV radiated area, the sample is exposed to

15 ppm mercury vapor for 16 hrs. Then the photoresist is removed, and the sample is checked by an optical microscope. Figure 5-6 shows the optical contrasts between mercury exposed areas and those of unexposed areas, where the bright regions have not been exposed to mercury vapor. This suggests that the adsorption of mercury on the gold nanoparticle arrays can be visualized in the microscopic level.

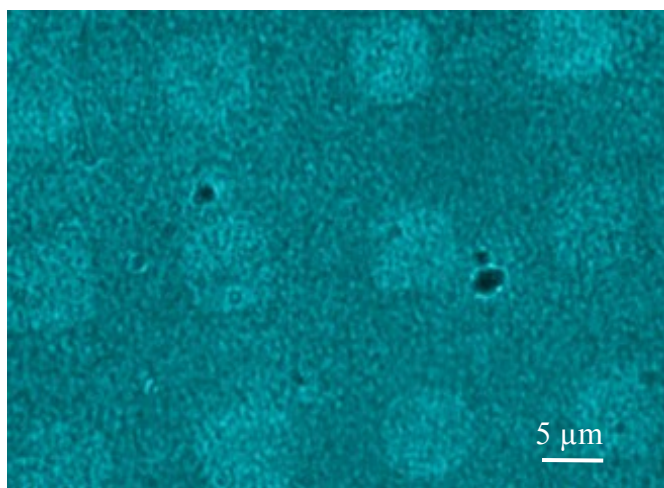


Figure 5-6 An optical micrograph of micropatterns produced in mercury vapor on a patterned substrate with gold nanoparticles, where the relative white areas are not exposed to mercury vapor.

Besides the positive contrast can be seen, a reversing contrast in photomask makes micropatterns with reversed contrast, which is shown in Figure 5-7A. In order to know the elements components in the exposed area, energy dispersive X-ray (EDX) spectroscopy is used and the results show that the circle contains gold and mercury (Figure 5-7B).

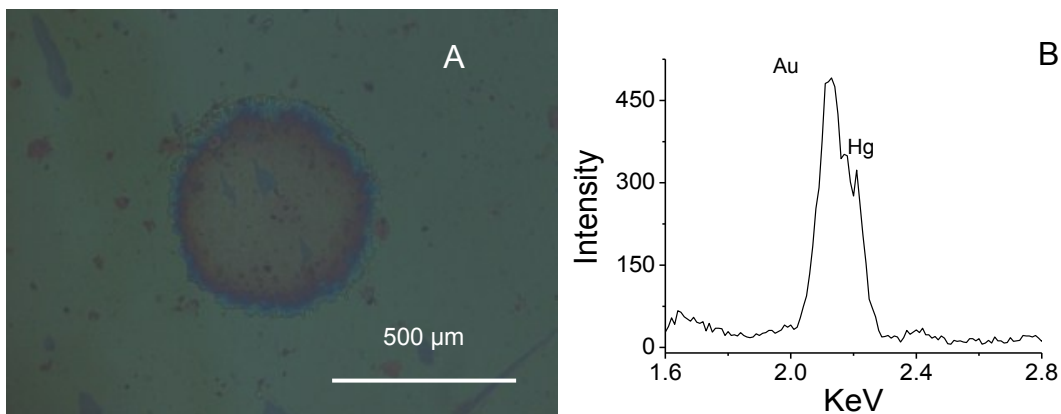


Figure 5-7 A micropattern produced on a glass substrate with gold nanoparticles in mercury vapor (B), where the circular area is exposed to mercury vapor; an EDX spectrum collected from a circle micropattern (C) after exposing to mercury vapor.

Except in make the pattern in microscale, a big pattern has also been made by using a lithography method on a substrate with gold nanoparticle arrays. If the pattern is large enough, the optical contrast can be seen clearly with naked eye. Figure 5-8 shows a “Hg” pattern on a glass slide with gold nanoparticle arrays, the relative white area wasn’t exposed to mercury vapor, while the rest of the area was exposed to saturated mercury vapor.

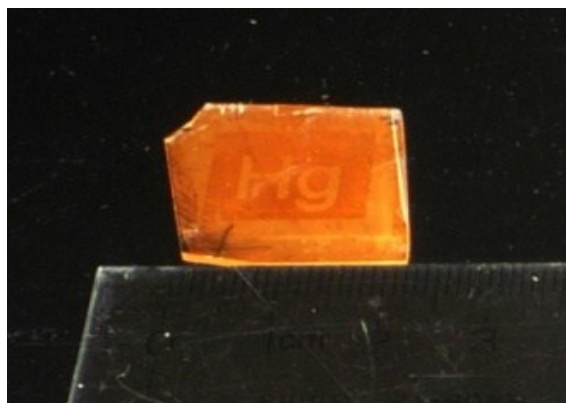


Figure 5-8 A graph of “Hg” character after exposing to mercury vapor on a $2 \times 2 \text{ cm}^2$ glass with an ordered array of gold nanoparticles.

The blue shift of plasmon peak upon adsorption of metal vapor is general. Indium powder is heated to 600°C and carried into the detection chamber by a nitrogen flow. Upon exposure to indium vapor, the plasmon peak of gold nanoparticles shifts to short wavelength direction as the exposure increases (Figure 5-9)

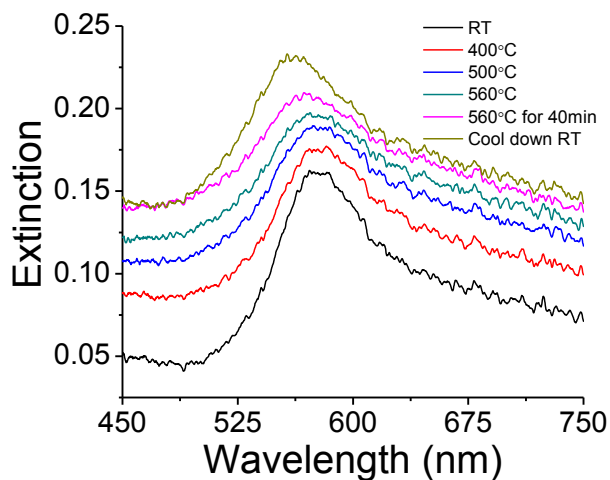


Figure 5-9 Extinction spectra of gold nanoparticle arrays after exposed to indium vapor for different length of time.

Silver nanoparticles deposited on glass surfaces have been exposed to mercury vapor, where the peak shifts to short wavelength as well (Figure 5-10). Since mercury has a higher vapor pressure than most metals, the method of mercury detection using gold nanoparticles has high specificity.

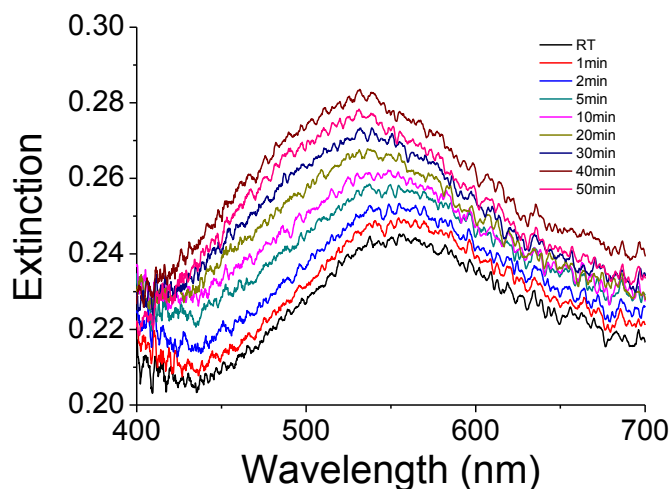


Figure 5-10 Extinction spectra of silver nanoparticle arrays after exposed to mercury vapor for different length of time.

Furthermore, gold nanoparticles can be deposited on a large glass surface to capture an appreciable amount of mercury while monitoring mercury concentration. We have made a large array of gold nanoparticles on a $7.5 \times 7.5 \text{ cm}^2$ glass substrate (Figure 5-11), which can be used as a window material to monitor and capture mercury vapor in air. If the nanoparticles contain 40% (mass ratio) of mercury, the mass of mercury that can be taken by nanoparticles on this glass is over 0.05 mg without effecting the appearance of the glass. Such numbers can reach 80 mg if surface area is increased to 10 m^2 . Providing that good circulation of air is maintained, 80 mg of mercury vapor floating in air can be captured on a 10 m^2 glass in 1 hour.

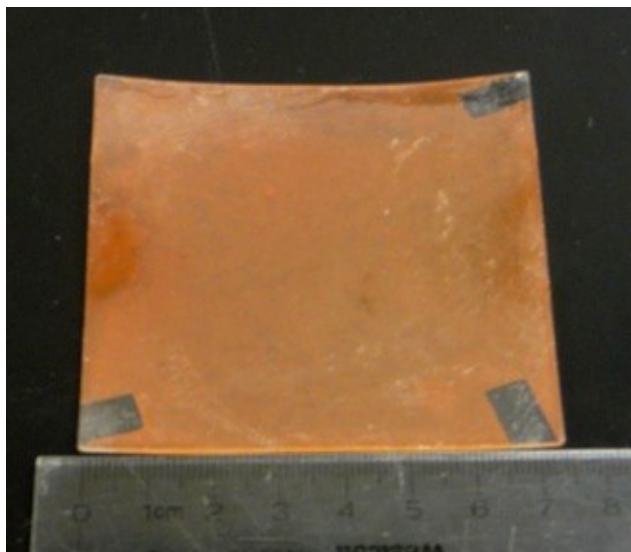


Figure 5-11 High temperature annealed gold nanoparticle arrays on a $7.5\text{cm} \times 7.5\text{cm}$ glass substrate.

5.3 Conclusions

In conclusion, molecular adsorptions on solid substrates can be sensitively and conveniently detected by shifts of localized surface plasmon resonance peaks. The peak shifts in cases of polymer film, mercury vapor, and DNT are sufficiently large in certain ranges that color changes can be directly visualized with naked eye. The gold nanoparticles can be regenerated after mercury adsorption, and can be produced over a large area to capture mercury in air. Compared to existing techniques of detecting chemical adsorption, this method involving plasmonic nanoparticles can be widely deployed to detect chemicals over a large area in a fast and convenient way. Meanwhile, structural engineering of nanoparticle array can further enhance the detection sensitivity.

CHAPTER 6: CONCLUSIONS

In summary, an ordered gold nanoparticle arrays with controlled size, shape, interparticle spacing and arrangement has been made by combining nanosphere lithography and thin film deposition. Plasmonic absorption peaks of thermally annealed gold nanoparticle arrays shift to long wavelength direction upon temperature increases up to 300°C and will return to original peak position after cooling down. A linear relationship exists between temperature and peak shift. The heating and cooling cycle can be repeated for many cycles. The thermal plasmonic properties of gold nanoparticles can be used to perform novel thermal analysis of adsorbed organic molecules with so-named plasmonic nano-balance. Not only can the mass of adsorbed materials can be detected, but the desorption process induced by temperature rise can also be detected. The plasmonic substrate can be regenerated after temperature-programmed rise and reused. Furthermore, the adsorption of the materials can be directly visualized by color changes of gold nanoparticle arrays. All of these results suggest the great potential of nanoparticle arrays for further applications.

REFERENCES

1. Rothenhausler, B.; Duschl, C.; Knoll, W., Plasmon surface polariton fields for the characterization of thin-films. *Thin Solid Films* **1988**, *159*, 323.
2. Zervas, M. N., Surface-plasmon polariton waves guided by thin metal-films. *Opt. Lett.* **1991**, *16*, 720.
3. Weeber, J. C.; Krenn, J. R.; Dereux, A.; Lamprecht, B.; Lacroute, Y.; Goudonnet, J. P., Near-field observation of surface plasmon polariton propagation on thin metal stripes. *Phys. Rev. B* **2001**, *64*.
4. Muller, K. G.; Veith, M.; MittlerNeher, S.; Knoll, W., Plasmon surface polariton coupling with dielectric gratings and the thermal decomposition of these dielectric gratings. *J. Appl. Phys.* **1997**, *82*, 4172.
5. Faryad, M.; Hall, A. S.; Barber, G. D.; Mallouk, T. E.; Lakhtakia, A., Excitation of multiple surface-plasmon-polariton waves guided by the periodically corrugated interface of a metal and a periodic multilayered isotropic dielectric material. *J. Opt. Soc. Am. B* **2012**, *29*, 704.
6. Faryad, M.; Lakhtakia, A., Grating-coupled excitation of multiple surface plasmon-polariton waves. *Phys. Rev. A* **2011**, *84*.
7. Mackay, T. G.; Lakhtakia, A., Surface-plasmon-polariton waves guided by the uniformly moving planar interface of a metal film and dielectric slab. *Optik* **2012**, *123*, 49.
8. Weiner, J., Phase shifts and interference in surface plasmon polariton waves. *Opt. Express* **2008**, *16*, 950.

9. Juluri, B. K.; Zheng, Y. B.; Ahmed, D.; Jensen, L.; Huang, T. J., Effects of geometry and composition on charge-induced plasmonic shifts in gold nanoparticles. *J. Phys. Chem. C* **2008**, *112*, 7309.
10. Chapman, R.; Mulvaney, P., Electro-optical shifts in silver nanoparticle films. *Chem. Phys. Lett.* **2001**, *349*, 358.
11. Wieczorzak, E.; Hamel, R.; Chabot, V.; Aimez, V.; Grandbois, M.; Charette, P. G.; Escherl, E., Monitoring of native chemical ligation on solid substrate by surface plasmon resonance. *Biopolymers* **2008**, *90*, 415.
12. Zheng, Y. B.; Jensen, L.; Yan, W.; Walker, T. R.; Juluri, B. K.; Huang, T. J., Chemically tuning the localized surface plasmon resonances of gold nanostructure arrays. *J. Phys. Chem. C* **2009**, *113*, 7019.
13. Whitney, A. V.; Elam, J. W.; Zou, S. L.; Zinovev, A. V.; Stair, P. C.; Schatz, G. C.; Van Duyne, R. P., Localized surface plasmon resonance nanosensor: A high-resolution distance-dependence study using atomic layer deposition. *J. Phys. Chem. B.* **2005**, *109*, 20522.
14. Coello, V.; Bozhevolnyi, S. I., Surface plasmon polariton excitation and manipulation by nanoparticle arrays. *Opt. Commun.* **2009**, *282*, 3032.
15. Rhodes, C.; Franzen, S.; Maria, J. P.; Losego, M.; Leonard, D. N.; Laughlin, B.; Duscher, G., Surface plasmon resonance in conducting metal oxides. *J. Appl. Phys.* **2006**, *100*, 054905.
16. Mulvaney, P., Surface plasmon spectroscopy of nanosized metal particles. *Langmuir.* **1996**, *12*, 788.

17. Jensen, T. R.; Malinsky, M. D.; Haynes, C. L.; Van Duyne, R. P., Nanosphere lithography: Tunable localized surface plasmon resonance spectra of silver nanoparticles. *J. Phys. Chem. B* **2000**, *104*, 10549.
18. Ghosh, S. K.; Nath, S.; Kundu, S.; Esumi, K.; Pal, T., Solvent and ligand effects on the localized surface plasmon resonance (lspr) of gold colloids. *J. Phys. Chem. B* **2004**, *108*, 13963.
19. Sherry, L. J.; Chang, S. H.; Schatz, G. C.; Van Duyne, R. P.; Wiley, B. J.; Xia, Y. N., Localized surface plasmon resonance spectroscopy of single silver nanocubes. *Nano Lett* **2005**, *5*, 2034.
20. Kim, S.; Jung, J. M.; Choi, D. G.; Jung, H. T.; Yang, S. M., Patterned arrays of au rings for localized surface plasmon resonance. *Langmuir* **2006**, *22*, 7109.
21. Mohapatra, S.; Mishra, Y. K.; Avasthi, D. K.; Kabiraj, D.; Ghatak, J.; Varma, S., Synthesis of gold-silicon core-shell nanoparticles with tunable localized surface plasmon resonance. *Appl. Phys. Lett.* **2008**, *92*.
22. Zhu, S. L.; Li, F.; Du, C. L.; Fu, Y. Q., A localized surface plasmon resonance nanosensor based on rhombic ag nanoparticle array. *Sensor. Actuat. B-Chem* **2008**, *134*, 193.
23. Mie, G., Contributions to the optics of turbid media, especially colloidal metal solutions. *Ann. Phys.* **1908**, *25*, 377.
24. Gulati, A.; Liao, H.; Hafner, J. H., Monitoring gold nanorod synthesis by localized surface plasmon resonance. *J. Phys. Chem. B* **2006**, *110*, 22323.
25. Tao, J.; Lu, Y. H.; Zheng, R. S.; Lin, K. Q.; Xie, Z. G.; Luo, Z. F.; Li, S. L.; Wang, P.; Ming, H., Effect of aspect ratio distribution on localized surface plasmon resonance extinction spectrum of gold nanorods. *Chin. Phys. Lett.* **2008**, *25*, 4459.

26. Kreibig, U.; Bour, G.; Hilger, A.; Gartz, M., Spectral properties and relaxation dynamics of surface plasmon electronic oscillations in gold and silver nanodots and nanorods. *J. Phys. Chem. B.* **1999**, *103*, 8410.
27. Sherry, L. J.; Jin, R. C.; Mirkin, C. A.; Schatz, G. C.; Van Duyne, R. P., Localized surface plasmon resonance spectroscopy of single silver triangular nanoprisms. *Nano Lett.* **2006**, *6*, 2060.
28. Hellmers, J.; Schmidt, V.; Wriedt, T., Improving the numerical stability of t-matrix light scattering calculations for extreme particle shapes using the nullfield method with discrete sources. *J. Quant. Spectrosc. Ra.* **2011**, *112*, 1679.
29. Draine, B. T.; Flatau, P. J., Discrete-dipole approximation for scattering calculations. *J. Opt. Soc. Am. A* **1994**, *11*, 1491.
30. Wu, Y.; Nordlander, P., Finite-difference time-domain modeling of the optical properties of nanoparticles near dielectric substrates. *J. Phys. Chem. C* **2009**, *114*, 7302.
31. McMahon, J. M.; Henry, A. I.; Wustholz, K. L.; Natan, M. J.; Freeman, R. G.; Van Duyne, R. P.; Schatz, G. C., Gold nanoparticle dimer plasmonics: Finite element method calculations of the electromagnetic enhancement to surface-enhanced raman spectroscopy. *Anal. Bioanal. Chem.* **2009**, *394*, 1819.
32. Dement'eva, O. V.; Rudoy, V. M., Colloidal synthesis of new silver-based nanostructures with tailored localized surface plasmon resonance. *Colloid J.* **2011**, *73*, 724.
33. Teranishi, T.; Eguchi, M.; Kanehara, M.; Gwo, S., Controlled localized surface plasmon resonance wavelength for conductive nanoparticles over the ultraviolet to near-infrared region. *J. Mater. Chem.* **2011**, *21*, 10238.

34. Zhang, X.; Hicks, E. M.; Zhao, J.; Schatz, G. C.; Van Duyne, R. P., Electrochemical tuning of silver nanoparticles fabricated by nanosphere lithography. *Nano Lett.* **2005**, *5*, 1503.
35. Kim, J.; Liu, G. L.; Lu, Y.; Lee, L. P., Spectral tuning of localised surface plasmon-polariton resonance in metallic nano-crescents. *Iee Proc-Nanobiotech* **2006**, *153*, 42.
36. Barbosa, S.; Agrawal, A.; Rodríguez-Lorenzo, L.; Pastoriza-Santos, I.; Alvarez-Puebla, R. n. A.; Kornowski, A.; Weller, H.; Liz-Marzán, L. M., Tuning size and sensing properties in colloidal gold nanostars. *Langmuir* **2010**, *26*, 14943.
37. Jeon, H. J.; Kim, K. H.; Baek, Y. K.; Kim, D. W.; Jung, H. T., New top-down approach for fabricating high-aspect-ratio complex nanostructures with 10 nm scale features. *Nano Lett.* **2010**, *10*, 3604.
38. Zheng, J.; Yang, R.; Xie, L.; Qu, J. L.; Liu, Y.; Li, X. G., Plasma-assisted approaches in inorganic nanostructure fabrication. *Adv. Mater.* **2010**, *22*, 1451.
39. Chang, C. H.; Tian, L.; Hesse, W. R.; Gao, H.; Choi, H. J.; Kim, J. G.; Siddiqui, M.; Barbastathis, G., From two-dimensional colloidal self-assembly to three-dimensional nanolithography. *Nano Lett.* **2011**, *11*, 2533.
40. Jain, T.; Westerlund, F.; Johnson, E.; Moth-Poulsen, K.; Bjornholm, T., Self-assembled nanogaps via seed-mediated growth of end-to-end linked gold nanorods. *Acs Nano* **2009**, *3*, 828.
41. Jeguirim, M.; Trouvé, G., Pyrolysis characteristics and kinetics of arundo donax using thermogravimetric analysis. *Bioresour. Technol.* **2009**, *100*, 4026.
42. Viswanathan, R.; Narasimhan, T. S. L.; Nalini, S., Vapor pressure measurements by mass loss transpiration method with a thermogravimetric apparatus. *J. Phys. Chem. B* **2009**, *113*, 8362.

43. Rhee, Y. M.; Head-Gordon, M., A delicate electronic balance between metal and ligand in [cu-p-cu-p] diamondoids: Oxidation state dependent plasticity and the formation of a singlet diradicaloid. *J. Am. Chem. Soc.* **2008**, *130*, 3878.
44. Hanafee, J. E.; Radcliff, S. V., Effect of high pressure on a strain gauge load cell. *Rev. Sci. Instrum.* **1967**, *38*, 328.
45. York, R. L.; Hologna, G. J.; Somorjai, G. A., Investigation of the influence of chain length on the interfacial ordering of l-lysine and l-proline and their homopeptides at hydrophobic and hydrophilic interfaces studied by sum frequency generation and quartz crystal microbalance. *Langmuir* **2009**, *25*, 9369.
46. Berger, R.; Gerber, C.; Gimzewski, J. K.; Meyer, E.; Guntherodt, H. J., Thermal analysis using a micromechanical calorimeter. *Appl. Phys. Lett.* **1996**, *69*, 40.
47. Stampfer, C.; Guttinger, J.; Roman, C.; Jungen, A.; Helbling, T.; Hierold, C., Electron shuttle instability for nano electromechanical mass sensing. *Nano Lett.* **2007**, *7*, 2747.
48. Zhou, J.; Lao, C. S.; Gao, P. X.; Mai, W. J.; Hughes, W. L.; Deng, S. Z.; Xu, N. S.; Wang, Z. L., Nanowire as pico-gram balance at workplace atmosphere. *Solid. State. Commun.* **2006**, *139*, 222.
49. Huang, Y. H.; Bai, X. D.; Zhang, Y., In situ mechanical properties of individual zno nanowires and the mass measurement of nanoparticles. *J. Phys.: Condens. Matter* **2006**, *18*, L179.
50. Zhao, X. Y.; Hrbek, J.; Rodriguez, J. A., The decomposition and chemistry of ru-3(co)(12) on tio2(110) studied with x-ray photoelectron spectroscopy and temperature programmed desorption. *Surf. Sci.* **2005**, *575*, 115.

51. Ostblom, M.; Liedberg, B.; Demers, L. M.; Mirkin, C. A., On the structure and desorption dynamics of DNA bases adsorbed on gold: A temperature-programmed study. *J. Phys. Chem. B* **2005**, *109*, 15150.
52. Millot, B.; Methivier, A.; Jobic, H., Adsorption of n-alkanes on silicalite crystals. A temperature-programmed desorption study. *J. Phys. Chem. B* **1998**, *102*, 3210.
53. Kariis, H.; Westermark, G.; Persson, I.; Liedberg, B., Infrared spectroscopic and temperature-programmed desorption studies of dimethylphenylphosphine adsorbed on the coinage metals. *Langmuir* **1998**, *14*, 2736.
54. Bertilsson, L.; Engquist, I.; Liedberg, B., Interaction of dimethyl methylphosphonate with alkanethiolate monolayers studied by temperature-programmed desorption and infrared spectroscopy. *J. Phys. Chem. B* **1997**, *101*, 6021.
55. Engquist, I.; Lundstrom, I.; Liedberg, B., Temperature-programmed desorption and infrared studies of d₂O ice on self-assembled alkanethiolate monolayers: Influence of substrate wettability. *J. Phys. Chem.* **1995**, *99*, 12257.
56. Biswal, S. L.; Raorane, D.; Chaiken, A.; Birecki, H.; Majumdar, A., Nanomechanical detection of DNA melting on microcantilever surfaces. *Anal. Chem.* **2006**, *78*, 7104.
57. Caruso, F.; Niikura, K.; Furlong, D. N.; Okahata, Y., Assembly of alternating polyelectrolyte and protein multilayer films for immunosensing. *Langmuir*. **1997**, *13*, 3427.
58. Kalyuzhny, G.; Schneeweiss, M. A.; Schanzer, A.; Vaskevich, A.; Rubinstein, I., Different plasmon spectroscopy as a tool for monitoring molecular binding to ultrathin gold films. *J. Am. Chem. Soc.* **2001**, *123*, 3177.

59. Lai, J. J.; Hoffman, J. M.; Ebara, M.; Hoffman, A. S.; Estournes, C.; Wattiaux, A.; Stayton, P. S., Dual magnetic-/temperature-responsive nanoparticles for microfluidic separations and assays. *Langmuir* **2007**, *23*, 7385.
60. Li, D.; Wieckowska, A.; Willner, I., Optical analysis of Hg^{2+} ions by oligonucleotide-gold-nanoparticle hybrids and DNA-based machines. *Angew. Chem. Int. Ed.* **2008**, *47*, 3927.
61. Nath, N.; Chilkoti, A., A colorimetric gold nanoparticle sensor to interrogate biomolecular interactions in real time on a surface. *Anal. Chem.* **2002**, *74*, 504.
62. Pohle, R.; Fleischer, M.; Meixner, H., In situ infrared emission spectroscopic study of the adsorption of H_2O and hydrogen-containing gases on Ga_2O_3 gas sensors. *Sens. Actuators. B* **2000**, *68*, 151.
63. Riboh, J. C.; Haes, A. J.; McFarland, A. D.; Yonzon, C. R.; Van Duyne, R. P., A nanoscale optical biosensor: Real-time immunoassay in physiological buffer enabled by improved nanoparticle adhesion. *J. Phys. Chem. B.* **2003**, *107*, 1772.
64. Selvaraju, T.; Das, J.; Jo, K.; Kwon, K.; Huh, C.-H.; Kim, T. K.; Yang, H., Nanocatalyst-based assay using DNA-conjugated Au nanoparticles for electrochemical DNA detection. *Langmuir* **2008**, *24*, 9883.
65. Sun, Y. G.; Xia, Y. N., Increased sensitivity of surface plasmon resonance of gold nanoshells compared to that of gold solid colloids in response to environmental changes. *Anal. Chem.* **2002**, *74*, 5297.

66. Tan, S.; Erol, M.; Sukhishvili, S.; Du, H., Substrates with discretely immobilized silver nanoparticles for ultrasensitive detection of anions in water using surface-enhanced raman scattering. *Langmuir* **2008**, *24*, 4765.
67. Yang, J.; Eom, K.; Lim, E.-K.; Park, J.; Kang, Y.; Yoon, D. S.; Na, S.; Koh, E. K.; Suh, J.-S.; Huh, Y.-M.; Kwon, T. Y.; Haam, S., In situ detection of live cancer cells by using bioprobes based on au nanoparticles. *Langmuir* **2008**, *24*, 12112.
68. Charles, Y. W.; Jin, R. C.; Mirkin, C. A., Nanoparticles with raman spectroscopic fingerprints for DNA and rna detection. *Science* **2002**, *297*, 1536.
69. Roberts, M. A.; Kelley, S. O., Ultrasensitive detection of enzymatic activity with nanowire electrodes. *J. Am. Chem. Soc.* **2007**, *129*, 11356.
70. Zheng, G. F.; Patolsky, F.; Cui, Y.; Wang, W. U.; M., L. C., Multiplexed electrical detection of cancer markers with nanowire sensor arrays *Nat. Biotechnol.* **2005**, *23*, 1294.
71. Haes, A. J.; Van Duyne, R. P., A nanoscale optical biosensor: Sensitivity and selectivity of an approach based on the localized surface plasmon resonance spectroscopy of triangular silver nanoparticles. *J. Am. Chem. Soc.* **2002**, *124*, 10596.
72. Malinsky, M. D.; Kelly, K. L.; Schatz, G. C.; Van Duyne, R. P., Chain length dependance and sensing capabilities of the localized surface plasmon resonance of silver nanoparticles chemically modified with alkanethiol self-assembled monolayers. *J. Am. Chem. Soc.* **2001**, *123*, 1471.
73. Morris, T.; Copeland, H.; McLinden, E.; Wilson, S.; Szulczewski, G., The effects of mercury adsorption on the optical response of size-selected gold and silver nanoparticles. *Langmuir* **2002**, *18*, 7261.

74. Yang, D.; Lu, H.-H.; Chen, B.; Lin, C.-W., Surface plasmon resonance of SnO_2/Au bi-layer films for gas sensing applications. *Sens. Actuators. B* **2010**, *145*, 832.
75. McNerney, J. J.; Buseck, P. R.; Roland, C. H., Mercury detection by means of thin gold films. *Science* **1972**, *178*, 611.
76. Sabri, Y. M.; Kojima, R.; Ippolito, S. J.; Wlodarski, W.; Kalantar-zadeh, K.; Kaner, R. B.; Bhargava, S. K., Qcm based mercury vapor sensor modified with polypyrrole supported palladium. *Sensor Actuat B-Chem* **2011**, *160*, 616.
77. Kenduzler, E.; Ates, M.; Arslan, Z.; McHenry, M.; Tchounwou, P. B., Determination of mercury in fish otoliths by cold vapor generation inductively coupled plasma mass spectrometry (cvg-icp-ms). *Talanta* **2012**, *93*, 404.
78. Liu, Y.; Kelly, D. J. A.; Yang, H.; Lin, C. C. H.; Kuznicki, S. M.; Xu, Z., Novel regenerable sorbent for mercury capture from flue gases of coal-fired power plant. *Environ. Sci. Technol.* **2008**, *42*, 6205.
79. Morel, F. M. M.; Kraepiel, A. M. L.; Amyot, M., The chemical cycle and bioaccumulation of mercury. *Annu. Rev. Ecol. Syst.* **1998**, *29*, 543.
80. Hrapovic, S.; Majid, E.; Liu, Y.; Male, K.; Luong, J. H. T., Metallic nanoparticle-carbon nanotube composites for electrochemical determination of explosive nitroaromatic compounds. *Anal. Chem.* **2006**, *78*, 5504.
81. Kawaguchi, T.; Shankaran, D. R.; Kim, S. J.; Matsumoto, K.; Toko, K.; Miura, N., Surface plasmon resonance immunosensor using Au nanoparticle for detection of TNT. *Sensor. Actuat. B-Chem* **2008**, *133*, 467.

82. Girotti, S.; Eremin, S.; Montoya, A.; Moreno, M. J.; Caputo, P.; D'Elia, M.; Ripani, L.; Romolo, F. S.; Maiolini, E., Development of a chemiluminescent elisa and a colloidal gold-based lfa for tnt detection. *Anal. Bioanal. Chem.* **2010**, *396*, 687.
83. Kolle, M.; Salgard-Cunha, P. M.; Scherer, M. R. J.; Huang, F.; Vukusic, P.; Mahajan, S.; Baumberg, J. J.; Steiner, U., Mimicking the colourful wing scale structure of the papilio blumei butterfly. *Nat. Nanotechnol.* **2010**, *5*, 511.
84. van Duffel, B.; Ras, R. H. A.; De Schryver, F. C.; Schoonheydt, R. A., Langmuir-blodgett deposition and optical diffraction of two-dimensional opal. *J. Mater. Chem.* **2001**, *11*, 3333.
85. Dimitrov, A. S.; Miwa, T.; Nagayama, K., A comparison between the optical properties of amorphous and crystalline monolayers of silica particles. *Langmuir* **1999**, *15*, 5257.
86. Dushkin, C. D.; Nagayama, K.; Miwa, T.; Kralchevsky, P. A., Colored multilayers from transparent submicrometer spheres. *Langmuir* **1993**, *9*, 3695.
87. Goodwin, J. W.; Ottewill, R. H.; Parentich, A., Optical examination of structured colloidal dispersions. *J. Phys. Chem.* **1980**, *84*, 1580.
88. Kralchevsky, P. A.; Nagayama, K., Capillary forces between colloidal particles. *Langmuir* **1994**, *10*, 23.
89. Kralchevsky, P. A.; Paunov, V. N.; Denkov, N. D.; Nagayama, K., Capillary image forces .1. Theory. *J. Colloid Interface Sci.* **1994**, *167*, 47.
90. Velev, O. D.; Denkov, N. D.; Paunov, V. N.; Kralchevsky, P. A.; Nagayama, K., Capillary image forces .2. Experiment. *J. Colloid Interface Sci.* **1994**, *167*, 66.

91. Denkov, N.; Velev, O.; Kralchevski, P.; Ivanov, I.; Yoshimura, H.; Nagayama, K., Mechanism of formation of two-dimensional crystals from latex particles on substrates. *Langmuir* **1992**, *8*, 3183.
92. Shuford, K. L.; Ratner, M. A.; Schatz, G. C., Multipolar excitation in triangular nanoprisms. *J. Chem. Phys.* **2005**, *123*, 114713.
93. Chiang, H. P.; Wang, Y. C.; Leung, P. T.; Tse, W. S., A theoretical model for the temperature-dependent sensitivity of the optical sensor based on surface plasmon resonance. *Opt. Commun.* **2001**, *188*, 283.
94. Draine, B. T.; Flatau, P. J. User guide for the discrete dipole approximation code ddscat.7.0 2009. <http://arXiv.org/abs/0809.0337v4>.
95. Dalacu, D.; Martinu, L., Temperature dependence of the surface plasmon resonance of au/sio₂nanocomposite films. *Appl. Phys. Lett.* **2000**, *77*, 4283.
96. Ha, J. M.; Solovyov, A.; Katz, A., Postsynthetic modification of gold nanoparticles with calix[4]arene enantiomers: Origin of chiral surface plasmon resonance. *Langmuir* **2009**, *25*, 153.
97. Mazur, M.; Michota-Kaminska, A.; Bukowska, J., Surface-catalyzed growth of poly(2-methoxyaniline) on gold. *Electrochim. Acta* **2007**, *52*, 5669.
98. Li, J.; Liang, K. S.; Camillone Iii, N.; Leung, T. Y. B.; Scoles, G., The structure of n-octadecane thiol monolayers self-assembled on au(001) studied by synchrotron x-ray and helium atom diffraction. *J. Chem. Phys.* **1995**, *102*, 5012.
99. Ozawa, T., A new method of analyzing thermogravimetric data. *Bull. Chem. Soc. Jpn.* **1965**, *38*, 1881.

100. Safaei, A.; Shandiz, M. A.; Sanjabi, S.; Barber, Z. H., Modeling the melting temperature of nanoparticles by an analytical approach. *J. Phys. Chem. C* **2007**, *112*, 99.
101. Steinfeld, J. I.; Wormhoudt, J., Explosive detection: A challenge for physical chemistry. *Annu. Rev. Phys. Chem.* **1998**, *49*, 203.
102. Snels, M.; Venezia, T.; Belfiore, L., Detection and identification of tnt, 2,4-dnt and 2,6-dnt by near-infrared cavity ringdown spectroscopy. *Chem. Phys. Lett.* **2010**, *489*, 134.
103. Aguilar, A. D.; Forzani, E. S.; Leright, M.; Tsow, F.; Cagan, A.; Iglesias, R. A.; Nagahara, L. A.; Amlani, I.; Tsui, R.; Tao, N. J., A hybrid nanosensor for tnt vapor detection. *Nano Lett.* **2010**, *10*, 380.
104. Preiss, A.; Elend, M.; Gerling, S.; Berger-Preiss, E.; Steinbach, K., Identification of highly polar nitroaromatic compounds in leachate and ground water samples from a tnt-contaminated waste site by lc-ms, lc-nmr, and off-line nmr and ms investigations. *Anal. Bioanal. Chem.* **2007**, *389*, 1979.
105. Schweyer, M. G.; Andle, J. C.; McAllister, D. J.; Vetelino, J. F., An acoustic plate mode sensor for aqueous mercury. *Sens. Actuators. B* **1996**, *35*, 170.
106. Huang, H. W.; Qu, C. T.; Liu, X. Y.; Huang, S. W.; Xu, Z. J.; Zhu, Y. J.; Chu, P. K., Amplification of localized surface plasmon resonance signals by a gold nanorod assembly and ultra-sensitive detection of mercury. *Chem. Commun.* **2011**, *47*, 6897.
107. Thundat, T.; Wachter, E. A.; Sharp, S. L.; Warmack, R. J., Detection of mercury-vapor using resonating microcantilevers. *Appl. Phys. Lett.* **1995**, *66*, 1695.

108. Sabri, Y. M.; Ippolito, S. J.; Tardio, J.; Atanacio, A. J.; Sood, D. K.; Bhargava, S. K., Mercury diffusion in gold and silver thin film electrodes on quartz crystal microbalance sensors. *Sens. Actuators. A* **2009**, *137*, 246.
109. George, M. A.; Glaunsinger, W. S., The electrical and structural properties of gold films and mercury-covered gold films. *Thin Solid Films* **1994**, *245*, 215.
110. Morris, T.; Szulczewski, G., A spectroscopic ellipsometry, surface plasmon resonance, and x-ray photoelectron spectroscopy study of hg adsorption on gold surfaces. *Langmuir* **2002**, *18*, 2260.